This is to certify that the

thesis entitled

AN AGE HARDENING STUDY OF A NEAR GAMMA TITANIUM ALUMINIDE Ti-47Al-2Nb-2Mn-0.08vol% TiB_2 ALLOYED WITH 0.1wt% CARBON

presented by

Raymond Joseph Simpkins II

has been accepted towards fulfillment
of the requirements for

MS degree in Materials Science Engineering

Thomas R Bieler
Major professor

Date 4/26/01

AN AGE HARDENING STUDY OF A NEAR GAMMA TITANIUM ALUMINIDE Ti-47Al-2Nb-2Mn-0.08vol% TiB_2 ALLOYED WITH 0.1wt% CARBON

By

Raymond Joseph Simpkins II

A THESIS

Submitted to
Michigan State University
In partial fulfillment of the requirements
for the degree of

MASTER OF SCIENCE

Department of Materials Science and Mechanics

2001

ABSTRACT

AN AGE HARDENING STUDY OF A NEAR GAMMA TITANIUM ALUMINIDE Ti-47Al-2Nb-2Mn-0.08vol% TiB_2 ALLOYED WITH 0.1wt% CARBON

By

Raymond Joseph Simpkins II

A classical age hardening study on a two-phase near gamma titanium aluminide with a composition Ti-47Al-2Nb-2Mn(at%)-0.08vol%TiB_2 +0.1wt%C has revealed an increase in primary creep resistance with increasing aging parameters. Solutionization experiments were conducted that revealed a solution temperature of 1300°C for 8 hours. Aging temperatures of 950°C, 1000°C, and 1100°C for 2 and 40 hours were conducted to study the effect of aging on precipitate size, morphology, distribution, and its effects on creep resistance. An increase in primary creep resistance with increasing precipitate size was observed with increasing aging time and temperature. Aging for 2 hours at each temperature produced microstructures yielding exceptional creep resistance compared to 40 hour aging times. Variation in primary creep resistance was traced to specimen location within each test bar. Specimens machined from the top of the test bar had greater primary creep resistance than specimens machined from the bottom of the test bar. This was correlated with microscopy that revealed large volume fractions of equiaxed gamma grains in the bottom 2/3 of cast test bars resulting from the closure of porosity during the HIP (hot isostatic pressing) heat treatment. Optical, scanning electron (SEM), and transmission electron microscopy (TEM) were used to characterize the microstructure resulting from the various aging schemes.

ACKNOWLEDGEMENTS

I would like to extend great thanks to my advisor, Dr. Thomas R. Bieler, for his guidance and patients throughout my graduate studies and completion of this thesis and giving me the opportunity to work on such a great project. I would also like to thank Dr. James Lucas and Dr. K.N. Subramanian for sitting as committee members for my masters defense.

I would like to extend thanks to the Howmet Research Center (Whitehall, MI) for funding this thesis and the use of their testing facilities. In particular, Paul McQuay, Don Clemens, and Thomas Tom of the Howmet Research Center, for their support throughout the time spent on this project. I would also like to thank the technicians at the Howmet Research Center for their help in processing the material used in this thesis.

Finally, I would like to thank my fellow graduate students who assisted me during my thesis work. Dr. John Heckman, for his help and time spent with me on the many hours of transmission electron microscopy performed for this thesis and Ben Simkin, for spending the time to teach me how to operate the scanning electron microscope.

TABLE OF CONTENTS

LIST OF TABLES

LIST OF FIGURES

"Images in this thesis are presented in color"

CHAPTER 1

Research of new materials to be used in high temperature environments has been of interest for many years. Over the past decade, near gamma titanium aluminides have attracted considerable attention as candidates for replacement of conventional superalloys in the aerospace and automotive industry as well as in land based gas turbine engines [1,2]. The metallurgical advances in alloy development has made it possible for near γ alloys to be produced which have relatively good oxidation resistance and exhibit excellent high temperature strength [3]. Table 1 compares various properties of titanium based alloys with conventional superalloys. The titanium aluminides best suited to meet the demands in high temperature environments are alpha-2 titanium alloys based on Ti_3Al, and gamma titanium aluminide alloys based on TiAl.

Table 1 Comparison of the properties of titanium aluminides, titanium based conventional alloys and superalloys reproduced from [1].

Property	Ti-Base Alloys	Ti3Al-Base Alpha-2 Alloys	TiAl-Base Gamma Alloys	Superalloys
Density (g/cm^3)	4.5	4.5-4.7	3.7-3.9	7.9-8.5
RT Modulus (GPa)	96-115	120-145	160-176	206
Yield Strength (MPa)	380-1150	700-990	400-630	-
Tensile Strength (MPa)	480-1200	800-1140	450-700	-
Creep Limit (°C)	600	750	1000	1090
Oxidation (°C)	600	650	900-1000	1090
Ductility (%) at RT	10-25	2-10	1-4	3-25
Ductility (%) at HT	12-50	10-20	10-600	20-80
Crystal Structure	hcp/bcc	$D0_{19}$	$L1_0$	fcc/$L1_2$

Before implementing near gamma titanium aluminides as replacements for conventional superalloys, a balance between high temperature strength and room temperature mechanical properties needs to be achieved. At present an inverse relationship between tensile properties and creep resistance exists as well as concern regarding the oxidation resistance at elevated temperatures [1,2]. To accomplish an optimal balance, an understanding of the relationships between the solubility of various phases present in the alloy and their contribution to the mechanical properties needs to be addressed. This can be achieved by focusing on the phase transformations that take place at elevated temperatures and their effect on the mechanical properties.

The addition of various alloying elements and their effect on phase stability and mechanical properties has improved the balance of various mechanical properties, particularly creep resistance and ductility [4]. Certain gamma alloys, which have displayed exceptional strength at elevated temperatures, have been developed using the XD™ process. Cast alloys produced by this method contain a TiB and TiB_2 particulate phase dispersed throughout the alloy [5]. The addition of carbon to XD™ gamma alloys has shown to improve the creep resistance of the alloy [6]. Aging studies have concluded that carbon serves as an interstitial solid solution strengthener and a carbide former. In both single phase and duplex near gamma alloys, the carbide precipitates have been observed to form in equiaxed γ-TiAl grains, around dislocations, and at the α_2/γ interface [7-10]. The precipitates that form have been identified as Ti_3AlC with the perovskite structure and spherical in shape and Ti_2AlC with an H-phase structure and rod-like morphology [11]. The aging studies that have been conducted to date have focussed on characterizing the precipitation phenomena in these alloys by noting the effect on the creep resistance and ductility. The process methodologies used in these studies incorporated aging schemes that would not be feasible from a production standpoint. In this thesis a classical age hardening study was conducted with the intent to obtain a heat treatment process that is cost effective and will take full advantage of the strengthening effects of the precipitates.

Chapter 2 is a literature survey that covers the basic physical metallurgy principles that govern the behavior of near-γ TiAl alloys. The crystal structure and microstructures of this class of alloys is discussed along with strengthening mechanisms and deformation behavior. Also in this chapter the principles governing the age hardening of metals are discussed. These principles lay the groundwork for the aging study conducted in this thesis. The proposed objective of this thesis is listed at the end of the chapter.

Chapter 3 is the experimental procedure followed during this investigation. Here the methods used to collect and reduce the data in this thesis are presented and are discussed in detail.

Chapter 4 discusses the first step in the aging process of a 47XD™ near-γ TiAl alloy containing 0.1wt% carbon. The solutionization of carbon in this alloy will be addressed by discussing the different solution heat treatments that were explored and their resultant microstructures.

In Chapter 5 the principles of classical age hardening that were given in Chapter 2 are applied to this family of alloys. A discussion of the aging temperatures and times selected and the result they had on room temperature properties and primary creep resistance will be addressed. The size and distribution of precipitates were examined for each aging heat treatment and compared to the creep resistance to help determine the most effective aging process.

Chapter 6 deals with a phenomenon that was encountered during the aging study. Typically a range of values showing high, medium and low data points for primary creep tests are observed. Primary creep data and microstructural observations revealed a relationship between specimen location and geometry with varying primary creep resistance. In this chapter an explanation will be given for this variation.

Chapter 7 concludes this thesis. Here the results from the previous chapters are summarized and recommendations for future work are presented.

CHAPTER 2
LITERATURE SURVEY

2.0 A Brief History of Gamma Titanium Aluminides

With the introduction of the J57 Turbojet Rotors in the middle 1950's, titanium based alloys have played an important role in the advanced performance capabilities of gas turbine engines [1]. Since their introduction, research surrounding the use of titanium aluminides for use in high temperature-high stress environments has been of interest. The first in-depth exploration of near gamma titanium aluminide alloys began in the 1970's and continued into the middle 1980's. Throughout this alloy development program, various alloy compositions were researched through wrought processing. The properties of interest in the early stages of these investigations were the room temperature ductility and creep resistance of the alloys. These early alloy development programs yielded microstructures that exhibited unfavorable primary creep resistance [2]. Towards the late 1980's a second major investigation of near gamma alloys was conducted. These alloys were produced through rapid solidification and wrought processing and exhibited similar microstructures. Using the data collected from the first investigation, improvements in the mechanical properties of the alloy system were accomplished through alloying additions [13]. With the knowledge of the effects of alloying elements and the processing routes used to produce the first generation of near gamma alloys, the second generation alloys showed potential for future use in high temperature environments [14].

During the past decade of alloy development, the primary focus has been to achieve a desirable balance in mechanical properties. As casting technology advanced and with an improved metallurgical understanding of the alloy system, gamma titanium aluminides were developed which illustrated exceptional high-temperature strength [15]. Table 2 lists the gamma alloys investigated over the past three generations of alloy development.

Table 2 Summary of high points in alloy development of near-gamma titanium aluminides reproduced from [15].

Generation	Compositions (at%)	Microstructure and Processing
First	Ti-48-1V-(0.1 wt.%C)	Fine-grained/Wrought/PM alloys
Second	Standard Alloys Ti-(45-48)Al-(1-2)M-(0-4)Nb M=Cr,Mn,V Modified Alloys Ti-(45-47)Al-(0-2)M-(0-5)X(0-2)Z X=Nb,Ta,W;Z=Si,B,Fe,N Ti-(45-47)Al-2Nb-2Mn+ (.8-7)vol.%TiB_2	FL/Duplex/Cast alloys Experimental/Wrought/P/M alloys FL/Duplex/Cast alloys Experimental/Wrought alloys Fine FL/Duplex/Cast alloys
Third	Wrought Alloys Modified for designed microstructures and solid solution hardening Ti-(45-47.5)Al-(1-2)M-(2-6)N-x(W,Hf,Sn,C)-(0-0.3)B Cast Alloys Same as wrought alloys Ti-(46-47.5)Al-2Cr-y(Nb,Ta)	Designed microstructure/Wrought alloys Duplex/NL/Casting alloys Casting duplex;nearly-lamellar Same as above

2.1 TiAl Phase Diagram, Microstructures, and Alloying Chemistry

2.1.1 TiAl Phase Diagram

Phase diagrams are an invaluable tool to the metallurgist. They allow the predictions of phase transformations at various temperatures and compositions and are indicators of phase stability. The majority of phase transformations that occur in the solid state emerge by thermally activated atomic movements. There are many different types of phase transformations that are caused by changes in temperature. Some of these transformations are precipitation reactions, ordering reactions, and eutectoid transformations.

The phase diagram for TiAl has been debated quite extensively over the past decade and these debates have focused primarily on the phase transformations of disordered α-Ti, β-Ti, and ordered α_2-Ti_3Al, and γ-TiAl [16-20]. Investigations of phase evolution have been made using solidification experiments, scanning electron microscopy (SEM), transmission electron microscopy (TEM), dilatometry, and high-temperature X-ray diffraction (XRD) analysis of alloys of various compositions which were heat treated at particular temperatures [18-21]. The compositions of the alloys in these experiments had a direct impact on the determination of the location of certain phase boundaries in the diagram [18]. With respect to the concentration of aluminum, alloys ranging in 46-50at%Al were hexagonal close-packed α-phase at elevated temperatures while alloys with less than 44at%Al were cubic β-phase over comparable temperature ranges [20]. The addition of alloying elements also impacted phase transformation. The β transformation temperature gradually decreased with increasing Nb and the martensitic transformation temperature also decreased with increasing Nb concentrations [22].

The majority of the phases present in the equilibrium phase diagram consist of disordered solutions with wide ranges of composition, or simple ordered structures that are based on the disordered solutions [16,23]. Disordered

HCP α-Ti becomes ordered in the DO_{19} structure to form Ti_3Al. At higher aluminum concentrations, ordered phases based upon the fcc structure of $TiAl_3$ and TiAl with the DO_{22} and $L1_0$ structures form respectively. In some conditions, other phases which form are the δ phase, $TiAl_2$, and an arrangement of antiphase structures based on the $L1_2$ structure [20].

The compositional range of the phase diagram for alloys that are currently being considered for high temperature applications is the portion containing 22at% to 66at% Al. The most widely accepted version of the phase diagram for near γ-TiAl alloys, based on observations made by McCullough *et al*, is depicted in Figure 1 below [19,20].

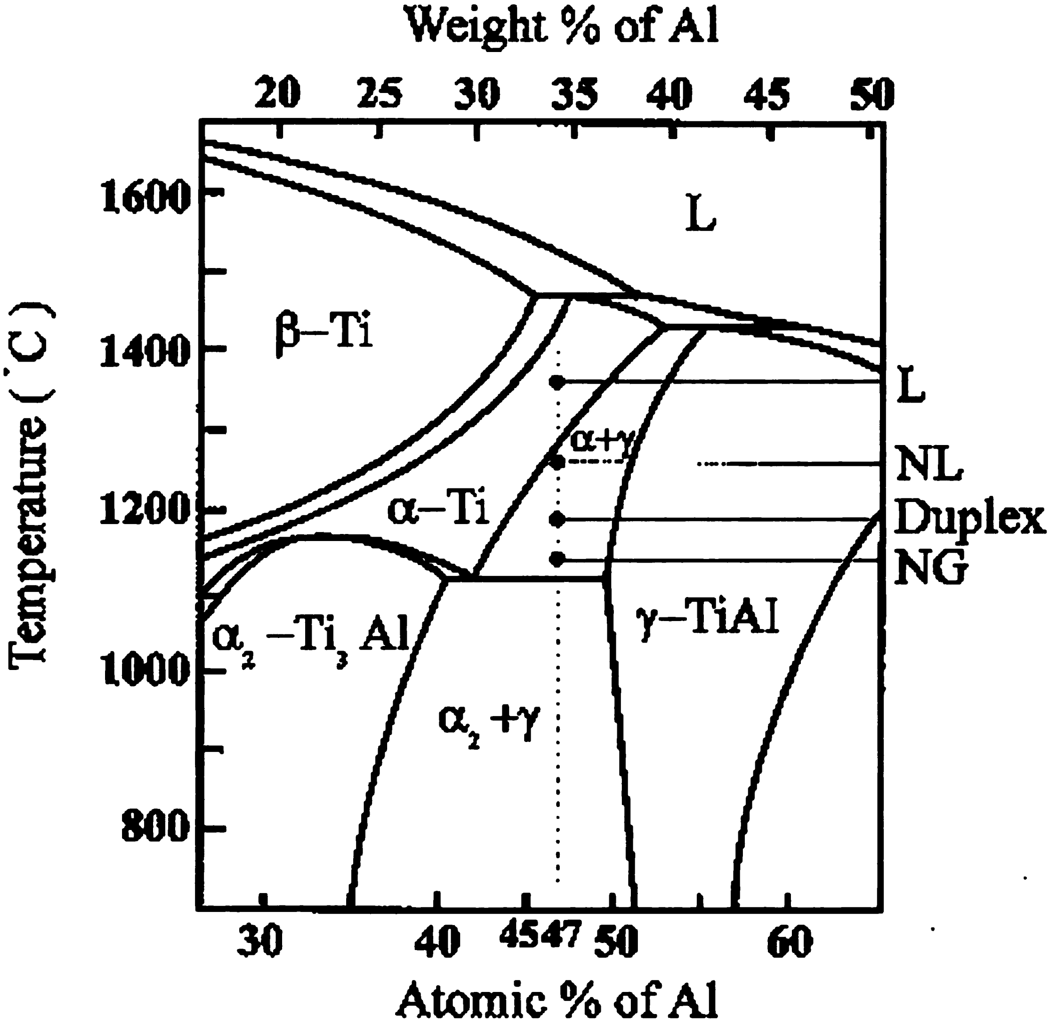

Figure 1 Ti-Al phase diagram showing the compositional range of interest for single and two phase γ-TiAl alloys reproduced from [25]. The phases of interest in this compositional range are the α_2-Ti_3Al and the γ-TiAl [24].

The α_2 phase has a compositional range extending from 22at% to 39at% Al where as the γ phase ranges in composition from approximately 48at% to 66at% Al [1,2,12]. Aluminum compositions between roughly 39at% to 50at% compose a two-phase region, Ti_3Al+TiAl. The stoichiometric compound has a c/a ratio of 1.015, which increases with increasing aluminum concentrations and decreases to 1.01 with decreasing aluminum [7].

Figure 2 depicts the atomic arrangements of the atoms in their respective crystal structures for the alloys in this region of the phase diagram. The γ-TiAl phase with the $L1_0$ crystal structure has alternating titanium and aluminum atoms stacked in an ABCABC sequence on the (002) planes. The α_2-Ti_3Al phase with the DO_{19} crystal structure has titanium and aluminum atoms stacked in an ABABAB stacking sequence [26,27].

Understanding the phase transformations that occur in this region of the diagram are important because of the impact that microstructure has on mechanical properties. The dotted line on the phase diagram is significant in that a variety of microstructures with exceptional high temperature strength can be obtained in the designated regions.

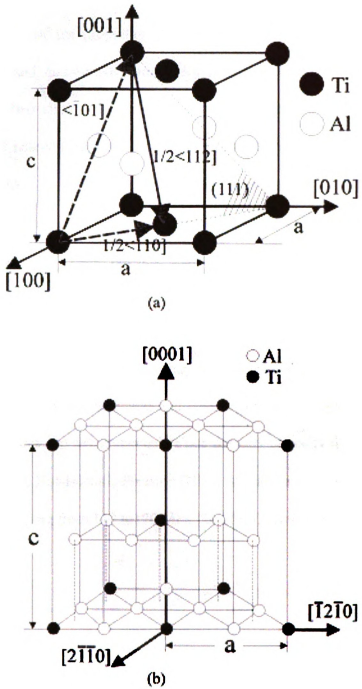

(a)

(b)

Figure 2 Atomic arrangements in the ordered f.c.t $L1_0$ crystal structure of γ-TiAl (a) and (b) in the ordered HCP DO_{19} crystal structure of α_2-Ti_3Al reproduced from [26, 27].

2.2.2 Formation of Microstructures

Many of the properties that make near γ-TiAl alloys attractive to the aerospace and automotive community can be inferred by its microstructure. There are two microstructural components in particular which contribute to the success of near-γ TiAl alloys, they are the single phase (γ) grains and two-phase lamellar (α_2 + γ) colonies. The microstructures found in the dashed compositional range of the phase diagram illustrated in Figure 1 can be classified into four groups. These are near gamma, duplex (composed of approximately equal volume fractions of gamma and lamellar grains), nearly lamellar, and fully lamellar. Figure 3 shows micrographs of the four types of microstructures that can be developed by heat treating the as-cast microstructure. The as-cast microstructure tends to be coarse and inhomogeneous. To homogenize the as-cast microstructures and simultaneously close porosity typically found near the center of the casting, Hot-Isostatic Pressing (HIP), typically around 1200°C (~2200°F) at pressures ranging from 140 to170 MPa (20-25ksi) for 4 hours, is employed.

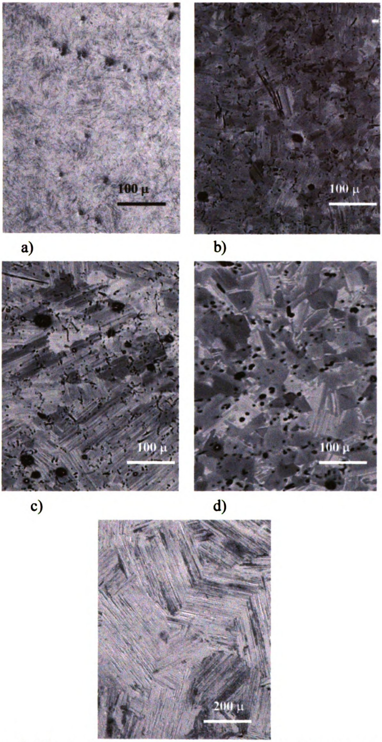

Figure 3 The evolution of the four different microstructures of gamma titanium aluminide, (a) as-cast ingot, (b) the duplex, (c) nearly lamellar, (d) near gamma, and (e) fully lamellar microstructure. Microstructures b-e received a Hot Isostatic Pressing (HIP) treatment.

The near γ microstructures are obtained by a long heat treatment just above the eutectoid temperature in the $\alpha + \gamma$ phase field. In this phase field a high volume fraction of the gamma phase is formed. The microconstituents formed are both coarse and fine γ grains that are pinned by α_2 particles. This microstructure is commonly non-uniform. The duplex microstructure consists of a mixture of equiaxed gamma grains and fine lamellar grains. This microstructure is typically the finest microstructure and is produced after a heat treatment at a temperature where gamma and alpha phases have equal volume fractions. Upon cooling, the α phase transforms to the lamellar microstructure where up to 6 variants of γ nucleate and grow along the α basal planes. The duplex microstructure yields the highest ductility but suffers in having a very low toughness and poor creep resistance [1, 2].

Nearly lamellar microstructures are produced by heat treatments near the alpha-transus [2,7]. This microstructure consists of predominantly coarse, lamellar grains that are transformed from the α grains and small fractions of fine gamma grains. The fully lamellar microstructure is composed of large grains and is produced by heat treating at temperatures above the alpha-transus. This microstructure displays large plate-like colonies of twin related γ-TiAl interspersed with α_2-Ti_3Al laths. Fully lamellar microstructures provide the best creep strength and fracture toughness compared to the duplex, but they have low ductility. Two noteworthy features of the lamellar structures are that refining the microstructure promotes ductility and allows further refinement by recrystallization of fine gamma grains [12].

There have been three types of lamellar structures identified that can form from subsequent heat treatments. These are the Type I, Type II, and Type III which have been distinguished through extensive microstructural experiments [28-30] as:

Type I:

$$\alpha \rightarrow \alpha + \gamma_P \rightarrow L(\alpha/\gamma) \rightarrow L(\alpha_2/\gamma)$$

Type II:

$$\alpha \rightarrow \alpha_2 \rightarrow \alpha_2 + \gamma_{Pt} \rightarrow \alpha_2 + \gamma_P \rightarrow L(\alpha_2/\gamma)$$

Type III:

$$\gamma_m + \alpha_2^P \xrightarrow{heating} \gamma_m + \alpha^P \rightarrow \gamma_m + \alpha_P \rightarrow L(\gamma/\alpha) \xrightarrow{cooling} L(\alpha_2/\gamma)$$

$$\gamma \xrightarrow{heating} \gamma_m + \alpha_{Pt} \rightarrow \gamma_m + \alpha_P \rightarrow L(\gamma/\alpha) \xrightarrow{cooling} L(\alpha_2/\gamma)$$

Type I and II are formed by the growth of γ-TiAl plates into the α or α_2-Ti_3Al phase in the two-phase region of the phase diagram shown in Figure 1. The γ-TiAl plates transform on the basal plane of the α_2-Ti_3Al and develop via the reactions involving the precipitation of the gamma plates. The crystal orientation of the γ plates vary from plate to plate within the lamellar grain. Type III lamellar structures have the same orientation relationship as type I and II. However, within type III lamellar structures, since all $\langle 11\bar{2}0 \rangle$ directions in α_2-Ti_3Al are equivalent, the crystal orientations of the γ plates are identical [28,30]. Microstructural studies conducted by Yamaguchi revealed that there are six possible orientation variants in accordance to the six possible orientations of the [110] on the (111) in the gamma phase of the lamellar grains with respect to the

$\langle 11\bar{2}0\rangle$ on (0001) in the α_2 phase [31-33]. These variants are illustrated in the stereographic projection given in Figure 4. The orientation relationships between the γ and α_2 laths in the lamellar grains is $\{111\}_\gamma \parallel (001)_{\alpha_2}$ and $<110>_\gamma \parallel <11\bar{2}0>_{\alpha_2}$ [7]. The twin related γ plates across the α_2 plates have both allowed [112] and forbidden [121] and [211] dislocations operating for the twin relation [34,35]. The $\{111\} < 11\bar{2}]$ twin relationship occurs most frequently than those without the true twinning orientation relationship. This is observed by the fact that true twinning of lamellar interfaces is more energetically favorable during the transformation of $\alpha \rightarrow \gamma$ [36].

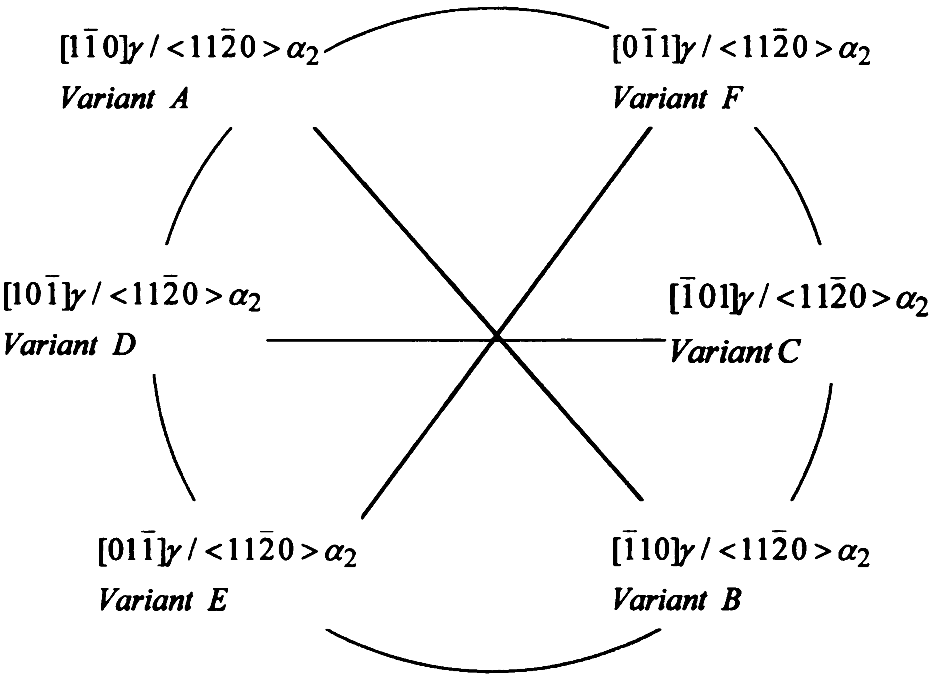

Figure 4 Stereographic projection showing the six possible orientation variants of γ with respect to α_2 in lamellar structures, reproduced from [33].

2.2.3 Alloying Chemistry

The addition of various elements to near gamma alloys has a profound impact on the properties of the alloy. Ternary additions of vanadium, manganese, molybdenum, and chromium increase the ductility in two-phase alloys and are also believed to reduce the oxidation resistance of gamma alloys [30,37-39]. These elements are also believed to shift the phase boundary toward the titanium side. Niobium, tantalum, tungsten, molybdenum, and those already mentioned strengthen the alloys by solid solution strengthening. Alloying with carbon, Si, B, Ni, and iron have been found to decrease the melt viscosity. Additions of carbon and Ni have shown to increase the creep resistance where B and Si additions show improved microstructural homogeneity [40,41]. Recently, minor additions of phosphorous, selenium or tellurium have been shown to increase the oxidation resistance [1,12]. Table 3 lists some of the alloying elements used in titanium aluminide production and their alloying effects.

Table 3 Common alloying elements used in near-γ TiAl alloys and their effects [1,12,15].

Elements	Effect
Al	Strongly effects ductility, best ductility occurs in range of 46-50 at% Aluminum.
B	Refines grain size and improves strength and workability (~0.5 at%).
C	Increases creep resistance and reduces ductility.
Cr	Increases the ductility in duplex alloys (1-3 at%), enhances the workability and superplacity (2 at%), greatly improves the resistance to oxidation (8 at%).
Er	Changes the deformation substructures and increases the ductility of single-phase gamma.
Fe	Increases fluidity but may lead to hot cracking at elevated concentrations
Mn	1-3 at% increases the ductility of duplex alloys.
Mo	Improves the ductility and strength of a fine-grained material and improves the oxidation resistance.
Ni	Increases fluidity.
Nb	Greatly improves the oxidation resistance and slightly improves the creep resistance.
P	Improves oxidation resistance
Si	Concentrations between 0.5-1 at% improve the creep and oxidation resistance, fluidity, and susceptibility to hot cracking.
Ta	Improves creep and oxidation resistance, increases the susceptibility to hot cracking.
V	Additions of 1-3 at% increases the ductility of duplex alloys but reduces oxidation resistance
W	Improves oxidation resistance and creep resistance
O	α stabilizer

2.3 XD™ Alloys

Advanced γ-based engineering alloys, which have displayed exceptional strength at elevated temperatures, have been developed using the XD™ process. Alloys developed by this process contain a TiB_2 particulate phase that produces a reinforced metal matrix composite. The addition of carbon to XD™ gamma alloys enhances high temperature mechanical properties such as creep resistance and promotes microstructural uniformity [4,14]. Much of the research that has been conducted to date has identified that volume fractions near 0.08 – 1.0%TiB_2 yield desirable mechanical properties [3]. The as-cast microstructures of near γ alloys containing TiB_2 have indicated two different morphologies of the particulate phase. A blocky TiB_2 morphology and wispy, needle like monoboride TiB [3,42].

2.4 Mechanical Properties and Deformation Mechanisms

2.4.1 Room Temperature Tensile Properties of Near-γ Alloys

The ductility of near-γ TiAl alloys has been of concern throughout its history of alloy development. The strength and ductility of near-γ alloys is a strong function of alloy composition and processing [7,15]. Due to the fact that near-γ alloys are brittle and that the deformation behavior of these alloys is predominantly controlled by crack propagation resistance, the tensile behavior of the alloy is often investigated. The room temperature yield strength (σ_Y) of two-phase γ-alloys usually is observed to range between approximately 300 to 650 MPa [30]. The yield strength depends on microstructure, grain and lamellar colony sizes, and has shown to be correlated with alloy chemistry [1,7]. Figure 5 is a stress-strain curve of various two-phase γ alloys. Alloys A, B, and C are forged Ti-47Al-1Cr-1V-2.5Nb which have a fully lamellar microstructure with colony sizes decreasing from 700-1300μm in alloy C to 250-500μm in alloy A. A general increase in yield strength was observed from approximately 300 MPa to 500 MPa as the lamellar colony size decreased from 1200 to 300 μm [30,43].

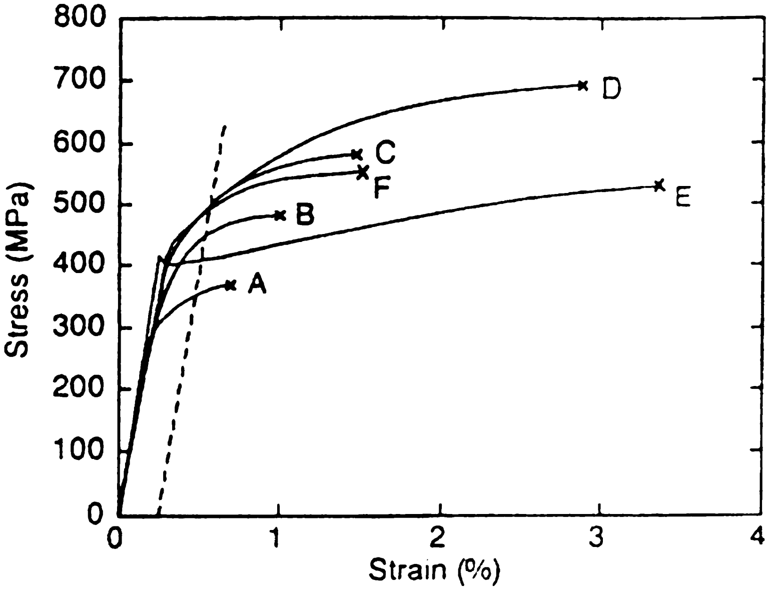

Figure 5 Stress-strain curves for various near γ alloys illustrating the dependence between RT ductility and microstructure. Alloys A-C are fully lamellar with decreasing colony size, alloy D is nearly-lamellar and alloy E represents a duplex microstructure, reproduced from [7].

Alloy D exhibited a nearly lamellar microstructure with lamellar colony sizes ranging between 70-140 μm and γ grains of 10-30 μm [30]. Alloy E represents a forged Ti-47Al-2Cr-0.2Si specimen exhibiting a duplex microstructure where alloy F was an investment cast and HIPed Ti-47Al-4%(Mn,Cr,Nb,B,Si) [7]. As mentioned earlier, the duplex microstructure yields the highest ductility which is observed in the figure above. Typical values for room temperature ductility range from ~2% to 3.5% depending on the composition of the alloy tested [44-46].

2.4.2 Elevated Temperature Tensile Properties of Near-γ Alloys

Depending on the microstructure and strain rate, the high temperature tensile ductility of two-phase γ-alloys is characterized by an abrupt brittle to ductile transition temperature (T_{tr}). For typical strain rates of $\dot{\varepsilon} \sim 1\times10^{-4}s^{-1}$, the T_{tr} ranges from approximately 620°C to 800°C. Figure 6 illustrates the variation in ductility as temperature is increased for the different microstructures of gamma alloys. From the figure it is noted that the brittle to ductile transition temperature for near gamma and duplex microstructures is low and it is high for fully lamellar structures [2,47-49].

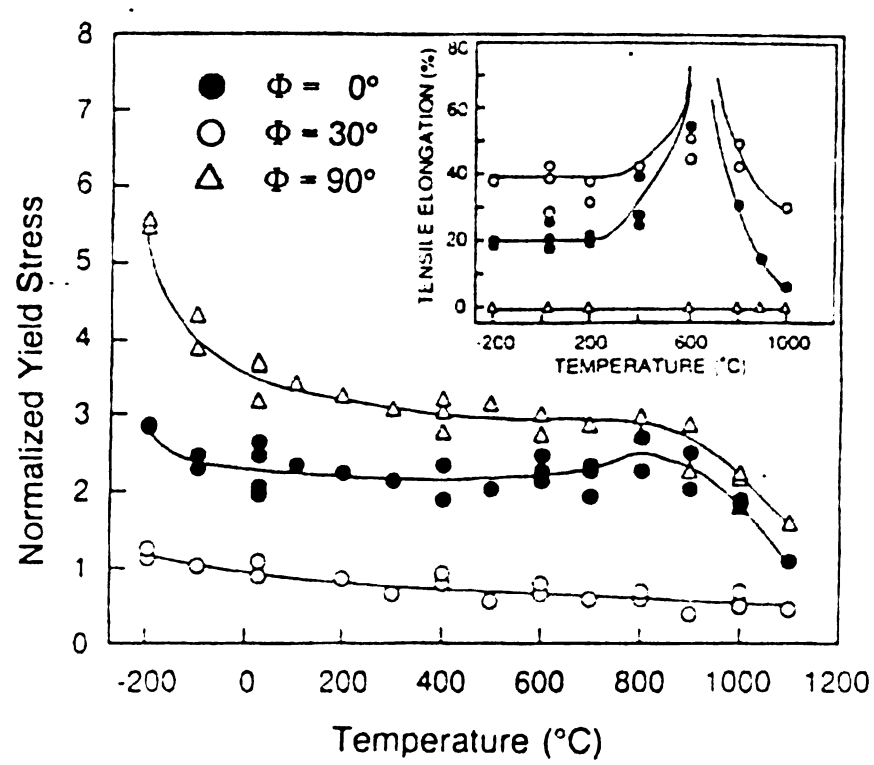

Figure 6 Difference in elevated temperature tensile ductility for the various microstructures of near gamma titanium aluminides, reproduced from [7].

Also, T_{tr} is controlled by thermally activated processes due to the distinct shift towards elevated temperatures with increasing strain rate [7]. The ductility is relatively constant below the brittle to ductile transition but it rises quickly with temperature above the T_{tr}. Alloys tested between 800°C and 900°C exhibit ductilites which exceeded 30% for duplex, near gamma, and fully lamellar microstructures [47-50].

2.4.3 Deformation Mechanisms of Near γ Alloys

The plastic deformation behavior of TiAl alloys is similar to deformation of other intermetallic compounds. These similar characteristics are the lack of ductility, temperature and orientation dependencies of the yield stress, and complex slip geometries [51-55]. The ordered intermetallic compound TiAl has a face-centered tetragonal structure with the $L1_0$ superlattice. The arrangement of atoms in the unit cell consists of alternating titanium and aluminum (002) planes stacked normal to the c-axis. The slip planes in γ-TiAl are the {111} close packed family of planes with the possible slip directions <110] and <101]. The mixed brackets are used as a reminder that the [110] slip direction is distinctly different from [101] directions due to the ordered lattice shown in Figure 2. The ordinary dislocations in this slip system are the ½ <110> dislocations and superdislocations of <011> and ½ <211> that leave the superlattice undisturbed [1]. The superdislocation core can dissociate into complex partial dislocations which are energetically more favorable. These partial dislocations are the $\frac{1}{6}[211] + \frac{1}{6}[12\bar{1}]$

and the $\frac{1}{6}[121]+[\bar{1}12]$ [28,29]. As the superdislocations are extended, planar faults such as stacking faults and anti-phase boundaries are produced.

Plastic deformation as the result of twinning is an important deformation mode in gamma titanium aluminides because of its ordered superlattice structure [56-57]. Within TiAl, twinning on the $[11\bar{2}]\{111\}$ has been found to be an important deformation mode at temperatures ranging between 25°C and 1000°C. Studies have shown that only true twinning on the $<11\bar{2}]\{111\}$ can occur since twinning on the $<211]\{111\}$ disrupts the $L1_0$ superlattice [58-59]. Figure 7 illustrates potential slip and twinning systems in γ-TiAl. Of the three twinning directions shown in Figure 7, only $\mathbf{b}_3$ causes true twinning since the same kind of atom is mirrored on the plane beneath (denoted by the small cirlces).

During true twinning, four mono-layers of Ti_3Al are formed between the matrix and the twin related TiAl lamellae. To prevent any violation of symmetry in the superlattice, these layers of Ti_3Al must form before the TiAl twins [28,29,60]. The thickness and distribution of the lamellae vary from colony to colony and this variation in thickness and distribution of lamellae are believed to have an effect on the strength of the alloy [61].

Stacking faults can form at early stages of deformation and develop into twins. The movement of partial dislocations at the twin interface has indicated the growth of twins at the interface [62]. These stacking faults have the identical stacking sequence as the Ti_3Al structure and have been suggested to be nucleation sites for Ti_3Al [60,62]. This mechanism for formation suggests that during the ordering transformation, stacking faults were produced on the basal plane of the Ti_3Al. Thus the TiAl twins nucleated at the stacking faults and then grew along the basal plane of the Ti_3Al [60,29]. The sequence of formation of Ti_3Al between the TiAl matrix and TiAl twin is shown schematically in Figure 8.

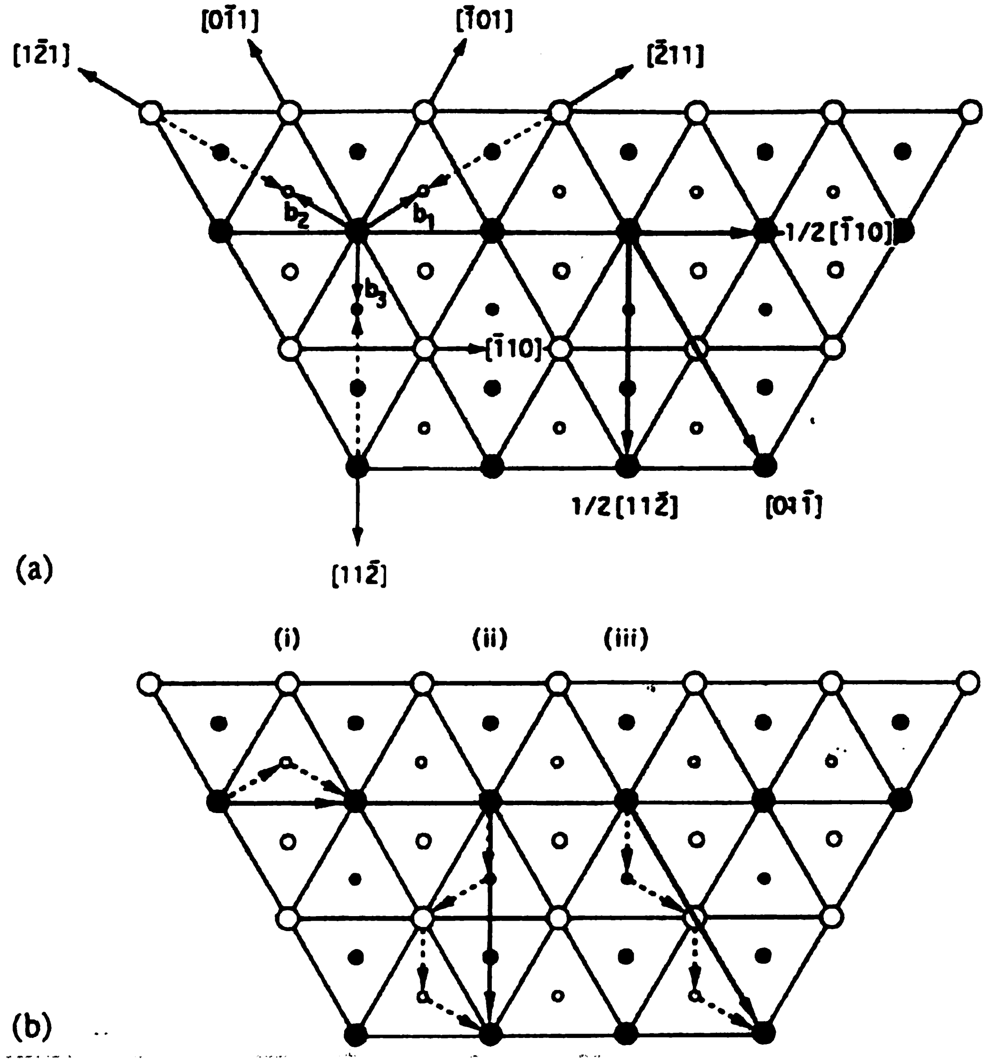

Figure 7 Possible slip and twinning systems for the $L1_0$ crystal structure showing a three layer sequence of atom stacking on the (111) plane. The open and shaded circles denote Ti and Al atoms, reproduced from [7].

| TiAl |

| TiAl | $\mathrm{TiAl_{SF}}$ | TiAl |

| TiAl | $\mathrm{TiAl_{SF}}$ | $\mathrm{Ti_3Al}$ | $\mathrm{TiAl_{SF}}$ | TiAl

| TiAl | $\mathrm{TiAl_{SF}}$ | $\mathrm{Ti_3Al}$ | $\mathrm{Ti_3Al_{SF}}$ | $\mathrm{Ti_3Al}$ | $\mathrm{TiAl_{SF}}$ | TiAl

| TiAl | $\mathrm{TiAl_{SF}}$ | $\mathrm{Ti_3Al}$ | $\mathrm{Ti_3Al_{SF}}$ | $\mathrm{TiAl_{Twin}}$ | $\mathrm{Ti_3Al_{SF}}$ | $\mathrm{Ti_3Al}$ | $\mathrm{TiAl_{SF}}$ | TiAl

Figure 8 The formation of stacking faults and twins due to high temperature deformation of near-gamma alloys, reproduced from [60].

2.5 Creep Resistance of Near γ Alloys

Creep is usually described by an empirical power law relationship, which relates the stress dependence and the creep strain rate, by the equation

$$\dot{\varepsilon} = A\sigma^{n} \ \exp^{-Q/RT} \tag{2.1}$$

where A is a constant that is dependent on the temperature and microstructural details, σ is the applied stress, Q is the activation energy, R is the gas constant, T is the temperature, and n is the stress exponent, which can vary depending on the microstructure. When modeling creep behavior of metals, creep can be interpreted by the physical view that a strain hardening processes, or increase in dislocation density, is balanced by a time softening process (climb controlled dislocation annihilation) resulting in a microstructure with a constant dislocation density. This approach allows the stress and temperature dependencies of the creep rate to be rationalized so that the activation energies and stress exponents can be determined using elementary processes [63].

The creep behavior of near-gamma alloys is characterized by a continuously evolving microstructure and therefore a steady state approach cannot be used. From numerous investigations, a continuously changing microstructure causes different minimum creep rates [64].

Focusing on interpreting the underlying deformation mechanisms, careful attention has been paid in determining the different deformation states and their stress dependencies. Some of the values for the stress exponent have been reported to range from 1 at low stresses to 10 at higher stresses. Stress exponents above 2 are indicative of creep deformation controlled by dislocation motion.

Apparent activation energies for creep vary from 150 kJ/mol at low stresses to 400 kJ/mol at higher stresses [7,12].

2.6 The Influence of Microstructure on Creep

The applications for which near gamma TiAl alloys have been targeted require these materials to have excellent elevated temperature creep resistance. Numerous efforts to understand and describe this material's behavior in high temperature environments over the past decade has revealed a continuously evolving microstructure during the creep process [64,65]. Both single phase γ and two-phase α_2+γ alloys have been shown to depend significantly on microstructure [65,66]. In these and other studies, the sensitivity of near-γ microstructures have been characterized by noting the grain size and volume fractions of the microconstituents present, stress and temperature dependencies, as well as other issues such as lath spacing in lamellar grains [65,67-69]. The concentration of aluminum has also shown to be a contributing factor to the observed unstable microstructure [70]. Some of the noted microstructural features, which take place during creep, are pinning of ordinary dislocations due to thermally activated cross slip, mechanical twinning, and dynamic recrystallization [68,71].

Due to their low room temperature ductility and fracture toughness, single-phase γ alloy development has been limited. However, the two-phase alloys based on α_2+γ Ti_3Al have shown an acceptable balance of room temperature ductility and elevated temperature creep resistance when alloyed and processed properly [14,15].

Fully lamellar microstructures have been shown to have a higher creep resistance than duplex microstructures of the same alloy due to the decrease in the effective slip distance for dislocation movement [38,69,72,73]. One explanation for this observation is related to the fine spacing in the lamellar grains. It has been shown that a refined lamellar microstructure, i.e. a smaller spacing between γ/γ laths and α_2 lath thickness, increases creep resistance and elevated temperature strength [67,73,74].

The influence that microstructure has on the creep behavior of near-γ alloys can best be described by comparing the creep strain as a function of time and the strain-rate as a function of strain at a constant load for various microstructures as shown in Figure 9 and Figure 10. In Figure 9 the fully lamellar microstructure can be characterized by a short primary creep regime that is followed by a steady-state creep region where the equiaxed γ and duplex microstructures show a rapid transition to tertiary creep, which in this study accounted for over 75% of the creep life [65]. In Figure 10 the influence of lamellar volume fraction on creep rate is shown. Here it is shown that the minimum strain-rate does not decrease monotonically with the volume fraction of lamellar colonies. Instead, a maximum is exhibited around volume fractions of lamellar grains equaling 30% in a duplex microstructure [7].

The influence of mechanical twinning on the creep behavior of near gamma alloys has also been well documented [68,71,75]. It has been shown to be an important deformation mechanism during creep in both equiaxed γ-grains as well as γ lamellae [76]. Skrotzki *et al* observed that the fraction of twinned γ-

grains increased with increasing stress and strain and that in contrast to the lamellar spacing issues, the twin spacing of the γ-grains decreased. Hemker *et al* observed similar results and concluded that this suggested that twins might be nucleated by the misfit stresses that build up in the crystal by ordinary dislocation movement [74]. The propensity for twinning of γ-laths in the lamellar grains was lower than in the equiaxed γ-grains due to the increased strength of the lamellar structure compared to the equiaxed gamma grains [74,76].

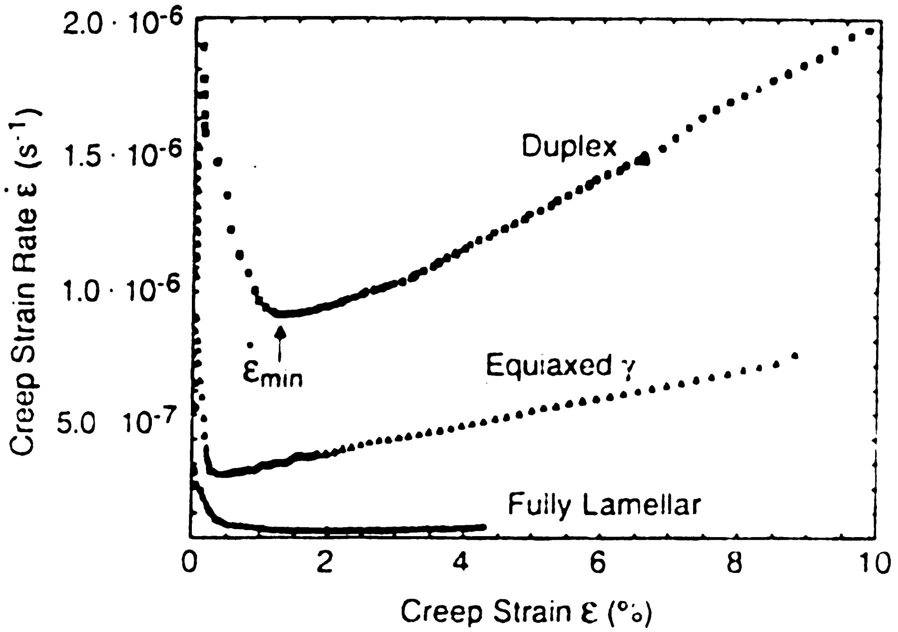

Figure 9 The influence that microstructure has on the creep behavior in near gamma TiAl alloys, reproduced form [65].

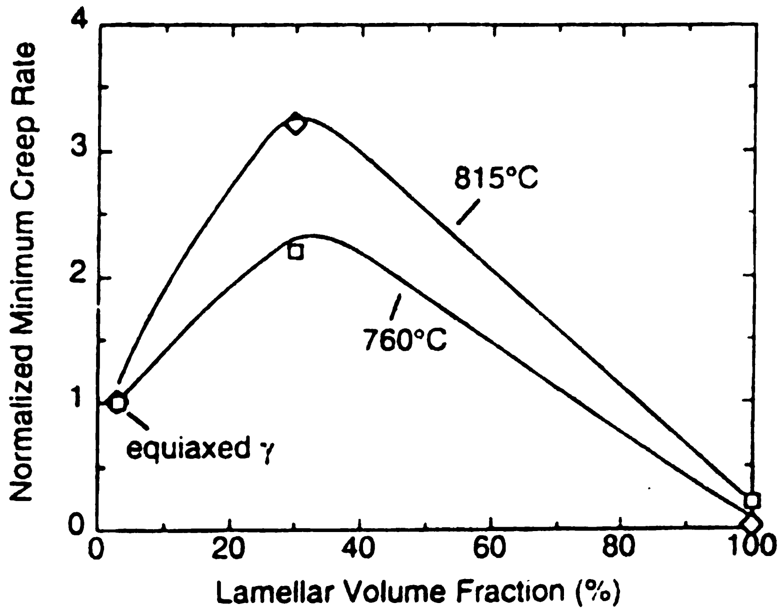

Figure 10 The influence of lamellar volume fraction on minimum creep rate, reproduced from [66].

2.7 Strengthening Mechanisms of Near-Gamma TiAl

Issues that describe the factors that contribute to the mechanical behavior of titanium aluminides have been discussed in previous sections. The strength requirements for engineering applications using near γ alloys has required implementation of metallurgical strengthening techniques. Some of those that have been explored involve grain refinement, solid solution and precipitation hardening. Results have indicated that combinations of all of these are beneficial [7,12,15]. In this section grain refinement and solid solution strengthening will be discussed briefly with more emphasis on precipitation hardening, since the theory behind this mechanism is significant to the subject matter in the preceding chapters.

2.7.1 Grain Refinement

Of the technical applications for which titanium aluminides have drawn considerable attention, the polycrystalline microstructure is much more producable than single crystals. Metallurgical principles state that the yield and fracture stresses increase as the grain size decreases. Therefore attention has been drawn to the effect of grain size on the material strength of near-γ alloys. For these reasons, the strength properties are frequently described in terms of Hall-Petch relations.

The Hall-Petch model can be rationalized by a discussion of dislocation motion during deformation. As dislocations pile up at a grain boundary in one grain, sufficiently large stresses on the boundary are created, and the stress necessary to initiate glide in an adjacent grain becomes possible. The experimental data collected to date characterizes microstructures by grain size, lamellar colony size, and lamellar spacing and distribution [7].

The Hall-Petch approximations have yielded several classes of near-γ based alloys. For equiaxed grains, the Hall-Petch constant ranges typically between $k_y = 0.9\text{-}1.3$ MPa $m^{-1/2}$ [44,45]. However, particular problems surface in the analysis of duplex microstructures due to the fact that grain sizes of lamellar colonies and equiaxed γ grains differ. Other factors that further complicate the analysis of duplex materials are the relative contributions of the two constituent phases to the total deformation of the polycrystal. These difficulties also surface for the lamellar microstructure because the flow stress may depend on colony and domain size as well as the lamellar spacing [7,12].

2.7.2 Solid Solution Strengthening

In section 2.3.3 the effects of alloying elements on the mechanical properties of near gamma alloys was discussed. In this section, the effects of alloying specific elements and their role in solid solution strengthening found from recent alloy development programs will be addressed. The role of Cr, and Mn were investigated in a base line Ti-48Al alloy and it was found that both increased the ductility of the alloy [77]. Niobium has also been shown to increase the yield strength in certain near-γ alloys [1]. Solution strengthening effects of refractory metals such as W, Mo, and Si have been explored [4] and have shown to improve the creep resistance and oxidation resistance in γ alloys.

2.8 Precipitation Hardening

2.8.1 Precipitation Theory

Increasing the solute level in a particular age-hardenable alloy can yield increases in yield strength as well as creep resistance. Maximizing those elements that participate in the aging sequence and can be put into solution at the solution heat treatment temperature can optimize the strength of an alloy. Heat treating an alloy at a temperature at which more than one phase is stable can produce the nucleation and growth of a secondary or tertiary phase. The addition of a secondary or tertiary phase in an alloy can hinder dislocation motion by pinning dislocations and in turn increasing the strength.

Precipitation hardening or age hardening is a common strengthening mechanism used to improve the strength of materials. Precipitation hardening is accomplished by solution heat treating of an alloy at elevated temperatures followed by quenching the alloy to obtain a supersaturated condition. The alloy is then heat treated or aged at lower temperatures for specific amounts of time to precipitate the solute out of solution. The total contribution to the increase in strength from the precipitate phase depends on several factors such as the concentration of the precipitating solute atoms in the solvent lattice, the temperature and time that the alloy is aged, the size and distribution of the precipitate, and the type of precipitate formed.

2.8.2 Precipitation Hardening in γ-TiAl Alloys

In the past few years of researching strengthening mechanisms, studies have indicated that the solubility of interstitial elements in near-γ TiAl is significantly lower than the impurity contents of popular technical materials [78,79]. These observations stimulated investigations by which strengthening of γ alloys was attempted via precipitation hardening. In experiments conducted by Menand *et al.* the maximum solubility of oxygen in the gamma matrix of ternary alloys was determined to be 6 times less than the total oxygen content which often exceeds 1500 at. ppm. Thus the excess oxygen was expected to lead to the precipitation of oxides which impede dislocation motion, increasing the strength of the alloy. Kawabata *et al.* obtained a notable increase in the yield strength with oxygen additions of approximately 6000 at. ppm [80].

The influence of interstitial elements on strength and ductility has been well documented over the last several years. In numerous studies, the precipitation of carbides and nitrides and their effects on mechanical properties were investigated [6,9,10,65,68,69,81]. The room temperature ductility of binary gamma alloys showed an increase with nitrogen content up to 0.3 mass%. The strengthening effects were attributed to grain refinement and precipitation hardening [9]. The contribution of carbon additions to γ-TiAl was observed to increase the creep resistance [6] as well as the yield strength [65,69]. However, as the concentration of carbon increased it was observed that the room temperature ductility decreased [65,69]. Figure 11 shows the variation of yield stress for a binary γ alloy with different levels of carbon.

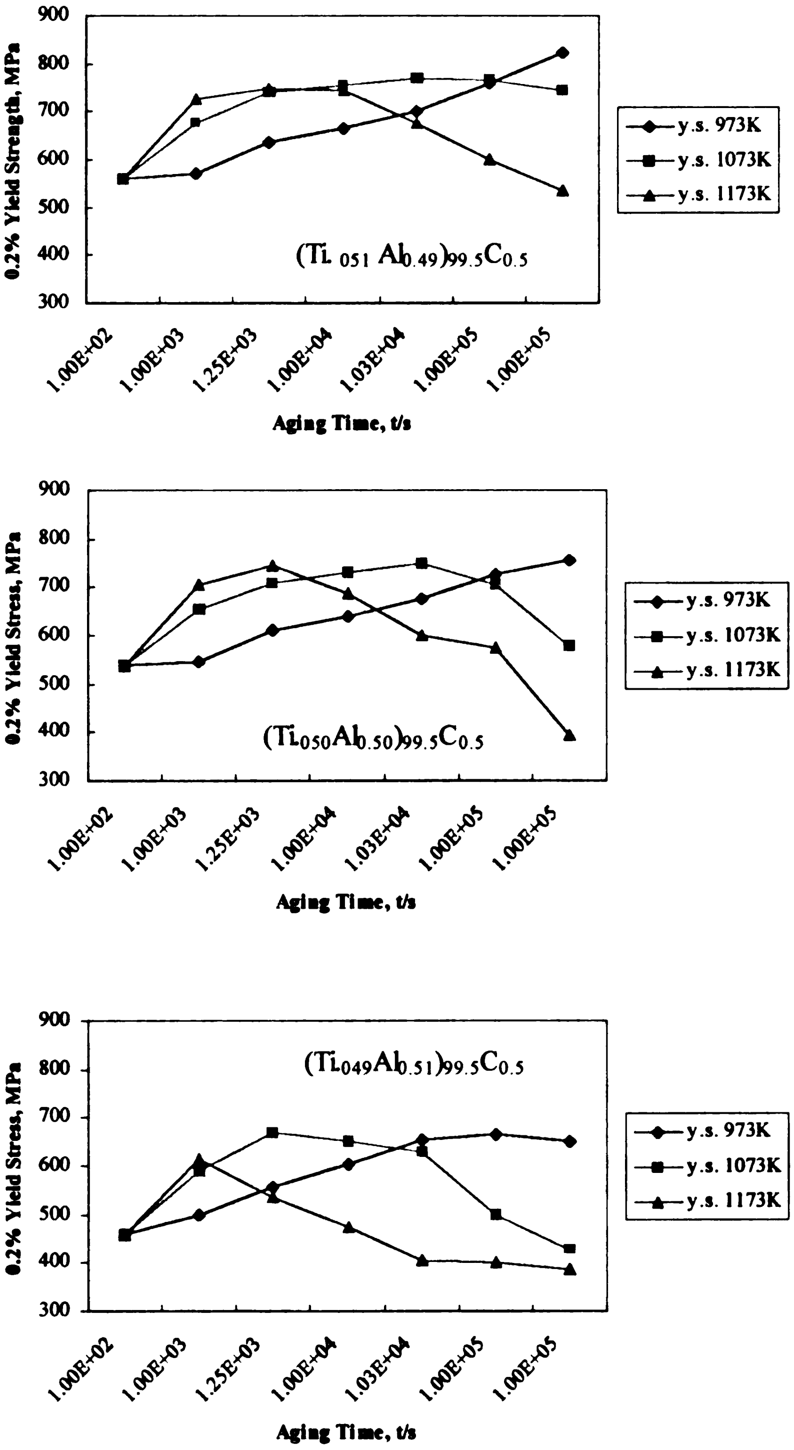

Figure 11 The effect of carbon additions on the yield strength a γ-TiAl alloy at elevated temperatures reproduced from [9].

Metallurgical principles indicate that for precipitate strengthening to be effective, a fine dispersion of precipitates is required. Both Tian *et al.* and Wagner detected fine dispersions of rod-shaped perovskite precipitates of the type Ti_3AlC and Ti_3AlN in binary γ alloys along with a hexagonal compound (H-phase) with the chemical formula Ti_2AlC [7,9]. Spherical precipitates were observed at lower aging temperatures while rod-like precipitates were observed at higher aging temperatures ($T_{age} > 1000°C$). These dispersions were formed by solutionizing and aging heat treatments, and were found to be very effective in improving the high temperature strength and creep resistance of the material [81]. From Figure 11 an overaged condition can be seen in the yield strength after significant aging times at 973K, 1073K, and 1173K. The behavior of these alloys agree with classical aging theory in that at low temperatures, long aging times are required before an overaged condition is observed and at higher temperatures the rate of age hardening increases significantly. Another important feature to note in Figure 11 is how the rate of age hardening is affected by aluminum concentration. Figure 12 shows the effects of deviation from stoichiometry on the yield strength of the alloys in Figure 11 [9]. From this figure it can be seen that the time to reach the maximum strength is related to the extent that the compositions of the alloys deviate from stoichiometry.

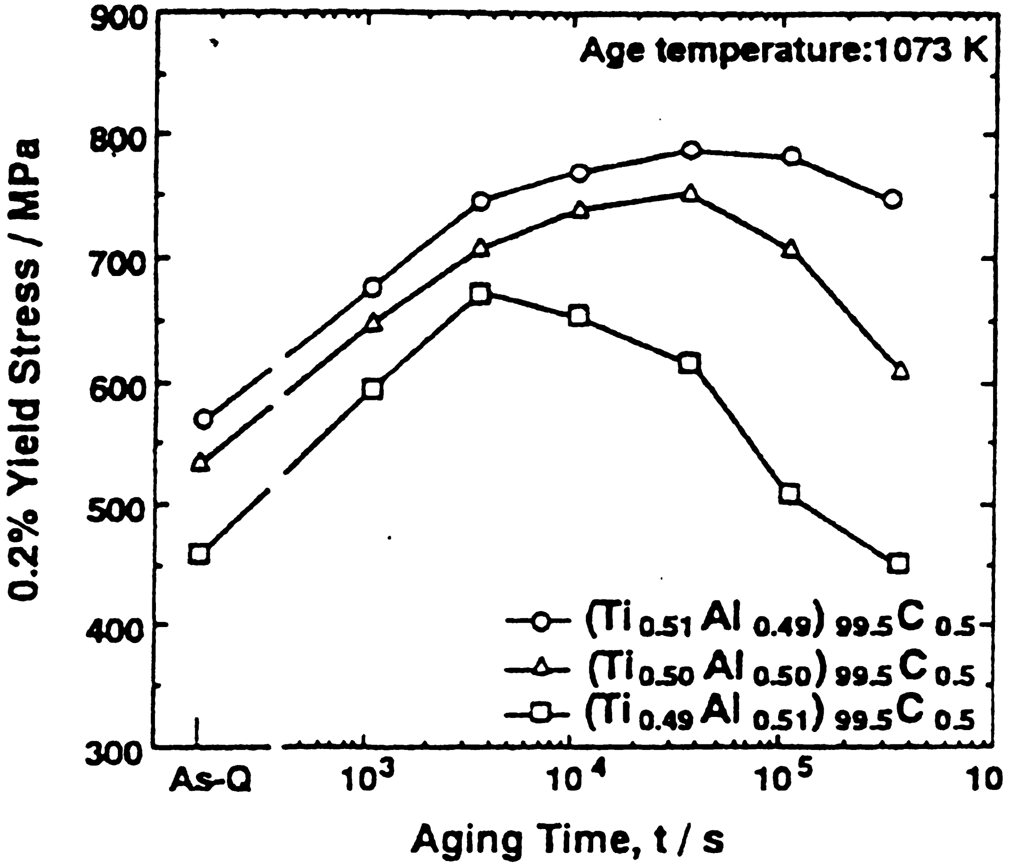

Figure 12 The variation in yield strength with deviation from stoichiometry, reproduced from [9].

Efforts to improve the high temperature strength of TiAl alloys have suggested that thermally activated glide and climb processes should be impeded [7,81]. The size of the elastic stress field associated with impurity related glide obstacles is therefore of interest. In studies by Appel and Christoph, γ alloys containing carbon in solution and in the form of perovskite precipitates were examined, and the dependence of the flow stress on the reciprocal of the activation energy was investigated. For the solutionized specimens, the flow stress was found to be independent of the carbon concentration, but with aging, the flow stress increased with carbon concentration.

This deformation behavior was exhibited in the activation volumes as well. At room temperature (1/V), where V was the activation volume, values were very large which suggested that the carbon atoms in solution acted as weak glide obstacles. These obstacles were easily overcome with the aid of thermal activation. Thus it was concluded that carbon in solution was an ineffective means of strengthening the material [81]. Figure 13 illustrates the dependency of the flow stress and the reciprocal activation volume with carbon concentration.

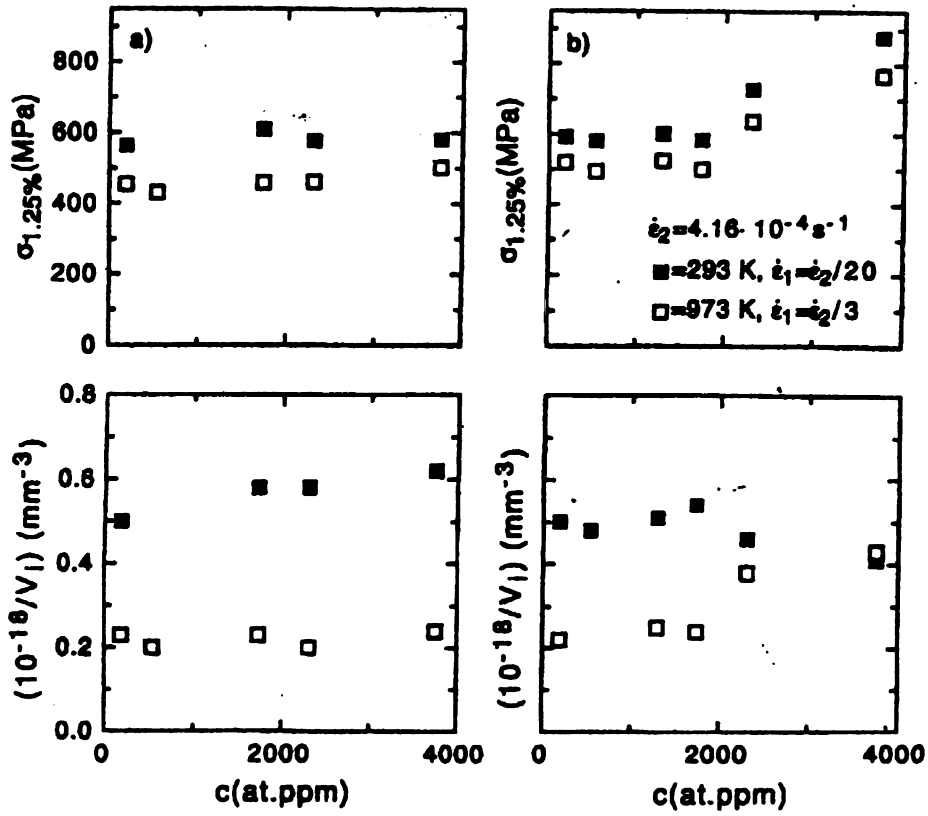

Figure 13 The relationship between the flow stress and the reciprocal of the activation volume of γ TiAl with carbon additions, reproduced from [7].

To determine the hardening mechanism of the precipitates, the orientation of the precipitates with its host matrix was determined. Dowling and Donlon observed rod-shaped Ti_3AlC precipitates with orientations of

$[100]_{ppt}//[100]_{TiAl}$, $[001]_{ppt}//[001]_{TiAl}$ [82].

The deformation structure that was observed after 3% compression tests at room temperature consisted of ½<110> ordinary dislocations and <011> superdislocations and $\frac{1}{6} < 11\bar{2}]$ ordered twins [81]. The perovskite structured precipitates were observed to pin the ordinary and partial dislocations that form twins. Appel *et al.* suggested that the observed bowing-out of the dislocation segments was caused by the high glide resistance of the perovskite structured precipitates. Figure 14 shows the bowing out of the dislocation between the precipitates.

It was concluded that a major portion of the total flow stress was attributed to the interaction of the ordinary and twinning partial dislocations with the precipitates. This view was supported by observations of sessile dislocation configurations and of immobilized deformation twins. Thus, hardening of two-phase titanium aluminides by precipitation of carbon out of solution was presumed to be an effective method of strengthening the material [6,8-10,81,82].

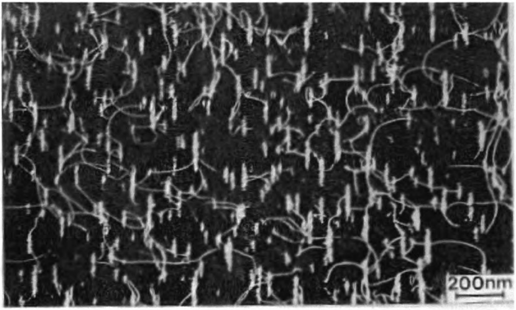

Figure 14 DF electron micrograph showing the dislocation interactions with the perovskite precipitates. Note the "bowing-out" of the dislocations, reproduced from [9].

2.9 Uncertainties of The Role of Carbon in Near-γ Alloys

The amount of carbon used in the aging studies conducted on near-gamma alloys has varied from small (.01at%C) to large (6.64at%C) concentrations [7,65,83]. Over the last decade of alloy development the main objective has been to improve the room temperature ductility of near-gamma alloys without compromising elevated temperature creep resistance. One issue that remains unresolved is the determination of the preferred concentration of carbon in two-phase gamma alloys so that the maximum strengthening effects of the carbide precipitates can be realized. In numerous studies focusing on the influence of carbon additions on the creep resistance of two-phase alloys, concentrations ranging from 0.05~ 0.3 at.%C show exceptional creep resistance [6,7,14]. Despite these findings, an adequate description of the aging behavior of near gamma alloys containing varying amounts of carbon as an interstitial alloying element is lacking.

The contribution of the carbide precipitates has not been evaluated at cost effective heat treatment temperatures and aging times, nor has a conclusion been drawn that clearly states whether or not carbide precipitates actually contribute significantly to the increase in creep resistance of two-phase near-γ alloys. Conflicting reports have indicated that carbon in solution promotes better creep resistance [69] where others have indicated that the carbide precipitates enhance the creep resistance [7]. Once these uncertainties can be explained, an understanding of the role that carbon can take in improving the performance of near-gamma titanium aluminides will be achieved.

3.0 Proposed Research

This investigation will focus on the balance between room temperature tensile properties and the high temperature creep resistance of a XD™ near-gamma titanium aluminide alloyed with two different concentrations of carbon. Throughout this investigation two issues that will be explored. First, the role that carbon plays in strengthening this intermetallic alloy will be evaluated. In order to understand the role that carbon plays in strengthening near-γ alloys, an optimal heat treatment process to obtain the maximum strengthening effects from the carbon additions needs to be explored. Before their contribution to the strength can be resolved, the carbon must be solutionized to dissolve the carbides formed during cooling from the HIP (Hot Isostatic Pressing) treatment. Classical age-hardening studies will then be conducted to determine a cost effective aging time and temperature to gain the maximum strengthening effects from the precipitates. Room temperature tensile tests will be conducted along with high temperature creep experiments to study the strengthening effects of the carbide precipitates. Both scanning electron microscopy (SEM) and transmission electron microscopy (TEM) techniques will be employed to characterize the precipitates by shape, size, and distribution within its host phase.

Secondly, based on the variability of properties observed in prior work, the effect of the specimen location within a casting on microstructure will be examined Mechanical test specimens made from near-γ alloys at the Howmet Corporation are done from investment castings of test bars. The size and geometry of the cast test bar determines the number of specimens that can be completed from a casting. For convenience, specimens machined from a single test bar are usually tested under the same parameters. When presenting mechanical test data it is not uncommon to see a range of values for specimens machined from the same test bar [9]. This result raises some important questions such as, whether or not the data is an adequate representation of the material's true behavior under the given test conditions, and could this variability be related to casting issues such as cast test bar geometry and gating issues.

The advances that have been made in alloy development and process technology over the past decade have indicated that all gamma components contain detrimental amounts of micro and macro porosity in the as-cast state [12,15]. In test bars this porosity is referred to as centerline porosity. For this reason as-cast microstructures require hot isostatic pressing (HIP) to close this porosity and further homogenize the microstructure. The region that contained the centerline porosity is commonly referred to as the centerline shrink area.

What has not been established from these advancements is the variation in microstructure that evolves from the HIP process, specifically the extent of equiaxed γ formation from the centerline shrink area to the edge of the cast test bars. Quantifying the amount of equiaxed grain transformation at different locations in the test bar may lead to an explanation of the variability seen in test data, since creep in near-gamma alloys is so sensitive to microstructure. This investigation may also give valuable insight to new gating designs that could alleviate the amount of porosity in the as-cast state for a specific geometry thus resulting in a more uniform microstructure after the HIP process.

CHAPTER 3
EXPERIMENTAL PROCEDURE

3.1 Introduction

This chapter discusses the processes used to collect the data presented in this thesis along with the methods used for data reduction. The procedures that were followed to produce the results will be discussed in the order in which they were implemented in the experiment. The guidelines used for conducting this study were based on classical age hardening theory.

3.2 Casting Process

Test bars of Ti-47Al-2Nb-2Mn(at%)+0.1wt%C-0.08vol%TiB_2 and Ti-45Al-2Nb-2Mn(at%)-0.08vol%TiB_2, (hereafter abbreviated 47XD™ and 45XD™), were investment cast at the Howmet Research Corporation (Whitehall, MI). The cast test bar geometry of the 47XD™ alloy was 203 mm (8 in) long with a constant 16mm (5/8 in) diameter. The cast geometry of the 45XD™ alloy was 178 mm (7 in) long tapering from 23mm (7/8 in) to 16mm (5/8 in) in diameter, hereafter called carrot shaped, and inverted carrot shaped having the same dimensions but cast with the smaller diameter at the top of the bar. Metal flow into the mold was from the top, with a riser above the mold to feed the casting as it solidified. All materials were hot isostatically pressed (HIPed) at 1260°C for 4 hours at 172 MPa to close porosity that was retained after casting. These castings were chosen to study how casting geometry is related to formation of porosity and the effect of HIP closure on the formation of equiaxed gamma grains in the test bars. The molds were wrapped in Kaowool and preheated before casting. All of the molds were investment cast in a induction skull remelt (ISR) furnace. The castings were removed from the furnace and were air cooled at room temperature. After cooling, the castings were given a HIP treatment at 1260°C for 4 hours at 172MPa to close porosity that was retained after casting.

3.3 Heat Treating

All of the heat treatments conducted for this experiment were performed at the Howmet Research Corporation (Whitehall, MI, U.S.A). Standard thermocouples connected to computerized data acquisition systems were employed to control the temperature and time of each heat treatment. The temperature at which the material was exposed determined what type of furnace was selected for the heat treatment. For heat treatments above 1100°C, a gas-fan cooled vacuum furnace was used. Argon gas was used as the quenching media to cool the specimens to room temperature. The cooling rate was set for 0.5°C/second. For heat treatments at or less than 1100°C a standard brick furnace with a maximum temperature capability of 1200°C was utilized. The quenching media used with these furnaces was oil.

In the solutionization experiment, test bars were exposed to various heat treatments in an attempt to obtain a homogenous solid solution and then quenched to room temperature to create a supersaturated condition of carbon in solution. The solution heat treatments that were explored are listed in Table 4.

Table 4 Times and temperatures used to determine solutionizing temperature of carbon in alloys investigated.

Solutionizing Temperature	Time (hrs)
1090°C (~2000°F)	1
1150°C (~2100°F)	1.5, 2
1230°C (~2250°F)	1, 2, 4
1300°C (~2370°F)	1, 2, 4, 8
1350°C (~2460°F)	1, 2, 4, 8

To examine the effect of aging on mechanical properties, aging heat treatments were conducted. The heat treatments used in this study are listed in Table 5. After solutionizing, aging heat treatments in the $\alpha_2+\gamma$ phase field, shown in Figure 1, were conducted at 950°C, 1000°C, and 1100°C ranging from 2 to 40 hours. A normalizing heat treatment (a heat treatment without solutionizing) was given to some specimens at 1010°C for 20 hours to stabilize the as-HIPed microstructure. Aging times of 1, 4 and 8 hours were also conducted to characterize the change in hardness with aging time. All heat treatments were conducted prior to specimen machining.

Table 5 Test matrix of heat treatments and aging times used to study the strengthening effects from carbon in a Ti-47Al-2Nb-2Mn-0.8vol%TiB_2 +0.07at%C.

Test Group	Aging Temperature	Aging Time (hrs)
I	As-HIPed	-
II	As-HIPed + 1010°C (1850°F)	20
III	950°C (~1740°F)	2, 4, 8, 40
IV	1000°C (~1830°F)	2, 4, 8, 40
V	1100°C (~2010°F)	2, 4, 8, 40

3.4 Metallography

3.4.1 Sample Preparation and Imaging

Microstructural information was collected from optical, scanning electron microscopy (SEM), and transmission electron microscopy (TEM). Optical microcopy was used to calculate volume fractions of the constituent phases resulting from the various heat treatments explored. Samples prepared for optical microscopy were mounted and mechanically polished up to 0.05 micron and viewed under polarized light using an Olympus PME3 optical microscope at 200X. Polaroid images were taken to capture the microstructures.

Scanning Electron microscopy (SEM) was performed to obtain grain and cluster sizes at the Howmet Research Center and at Michigan State University using a Cam Scan 44FEG scanning electron microscope at 20keV. Images were captured using Raptor FrameGrabber™ under secondary electron (SE) and backscatter electron mode (BSE). Sample preparation for SEM analysis required sections of each specimen to be mechanically polished using SiC paper up to 600 grit followed by electropolishing using a 6% perchloric acid and methanol solution at 248K (-25°C) at 20 volts [4]. All sections were cut using a JECO™ diamond saw cutter at a rate of 10in/min.

Transmission electron microscopy (TEM) of the as-HIPed, solutionized, and aged samples were used to characterize the size, shape, and distribution of precipitates. The thin foils examined were produced by machining specimens from different locations in the casting into approximately 0.7~1mm thick disks using a JECO™ diamond saw cutter. After machining the disks, 3mm diameter blanks were Electro-Discharge Machined (EDM) using a SPARK erosion unit. A brass tube with an inner diameter of 3mm was used to EDM the blanks. All foils produced were cut so that the foil normal was in the direction of flow of the casting and parallel to the stress axis. The blanks were then mechanically polished on a stationary belt sander using SiC paper from 240 to 600 grit. The final thinning of the foils was performed using a Tenupol-3 twinjet polisher. The electrolyte solution used to thin the foils was a 6% sulfuric acid in methanol held at 243K at a voltage of 15V [6]. The foils were examined in a HITACHI-800 Transmission Electron Microscope.

Selected area diffraction (SAD) and bright field and dark field imaging techniques were used to capture precipitate/host matrix information. This method was used to determine if the precipitates were solutionized and confirm that the precipitates observed after aging were identical to those observed in literature was taken from *Edington* [85]. To confirm the orientation relationship between the precipitate and the host matrix in the alloy, a pair of parallel directions in a pair of parallel planes was established. The orientation relationship of the carbides with its host matrix has been shown to be [7-10]

$$[100]_{ppt}//[100]_{TiAl},\ [001]_{ppt}//[001]_{TiAl}.$$

Bright field images of the [100] zone axis in several gamma grains from several different foils were recorded to see if any precipitates were visible. In as-HIPed and heat-treated samples the precipitates were confirmed by conducting the same approach. The morphology of the precipitates was determined by tilting the foils through a range of degrees and noting whether or not the shape changed. The $\mathbf{g} \cdot \mathbf{b}$ analysis was performed on grains containing precipitates to insure that the features seen were not edge-on dislocations and were in fact precipitates.

3.4.2 Grain Size and Volume Fraction Calculations

Grain and cluster size along with volume fraction of constituent phases was calculated from the optical and SEM micrographs. For grain size and cluster size calculations, lines were superimposed on SEM micrographs and the numbers and types of grains intersected by the line were counted. It was important not to count any grain more than once if it was intersected twice. An example of line placement for grain size is shown in Figure 15.

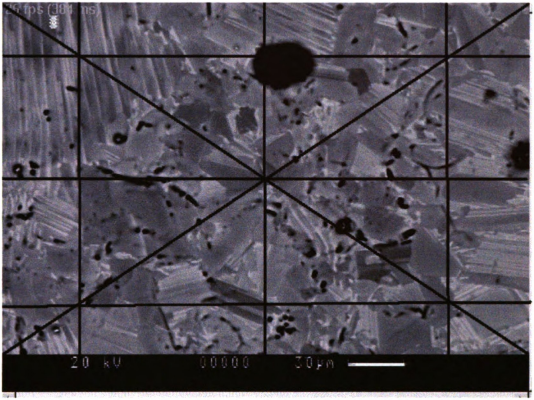

Figure 15 Line placement on micrographs to calculate grain size.

Once the number of grains were counted, the grain size was calculated by the relationship

$$grain\ \ size = \left(\frac{line\ \ length}{\#\, grains} \right) \times \left(\frac{Micron\ \ marker\ \ grainsize}{Line\ \ length\ \ of\ \ marker} \right) \qquad 3.1$$

The volume fraction of the constituent phases was calculated by superimposing a 10 cm^2 grid on micrographs taken from optical microscopy.

Every intersection of the grid on a particular phase was recorded. The volume fraction was then calculated using the equation

$$volume\ \ fraction = \left(\frac{\#\,grain\ \ \mathrm{int}\,er\sec ted\ \ on\ \ grid}{total\#\ \ \mathrm{int}\,er\sec tions\ \ on\ \ grid} \right) \times 100 \qquad 3.2$$

3.5 Mechanical Testing

As a first measure to determine an optimal aging temperature microhardness tests were performed using a LECO® M-400-G1 bench mounted hardness tester with an optical digital readout display that indicated the hardness. A load of 50g for 5 seconds at 55X was used to make the micro-indents across polished samples machined from test bars. Microhardness testing required that the specimens be polished up to 3 micron.

Room temperature tensile tests were performed by Metals Technology Incorporated (Northridge, CA, U.S.A). Stress-strain curves were recorded and the 0.2% yield strength, % elongation (%EL), and ultimate tensile strength (UTS) were reduced from the curves. Elevated temperature primary creep experiments were conducted at Howmet Research Center (Whitehall, MI, U.S.A). All creep tests were in tension and test data was recorded using a computerized data acquisition system configured specifically for the desired test.

Creep experiments on the 47XD™ specimens were conducted at 650°C (1200°F) with a tensile stress component of 40ksi (276 MPa) and at 815°C (1500°F) with a tensile stress component of 20ksi (138 MPa). The 45XD™ carrot and inverted carrot shaped specimens were tested at 700°C, 200 MPa, and 800°C, 100 MPa. All creep specimens were deformed up to 0.5% creep strain. After testing, the chemical composition was evaluated at various locations in the test bars to quantify the homogeneity throughout the castings. The raw creep data was taken from the data acquisition system and reduced using KaleidaGraph™ software. To obtain an accurate depiction of what was occurring in the material during primary creep, the θ-projection concept was utilized to reduce the creep data.

The original model, developed by Evans and Wilshire, is given by the equation [25],

$$\varepsilon = \varepsilon_1 + \theta_1\{1\text{-}\exp(-\theta_2 t)\} + \theta_3\{\exp(\theta_4)-1\} \qquad 3.3$$

where θ_1 and θ_3 define the strain magnitude with respect to time, t, and θ_2 and θ_4 describe the curvature of the primary and tertiary stages of a creep curve. The second term in Equation 3.3 represents strain hardening, which is dominant in primary creep while the third term embodies strain weakening, which is the mechanism dominating tertiary creep. Since secondary creep is only a transition between primary and tertiary and is explained on the basis of competing processes of both primary and tertiary creep, a true depiction of steady state creep cannot be estimated by Equation 3.3. For this reason Equation 3.3 was modified to obtain an accurate description of the deformation occurring during primary creep. The creep data in this experiment was reduced using a modified version of the θ-projection model derived to describe the primary and secondary stages of creep deformation in TiAl alloys [25].

$$\varepsilon_{\text{primary creep}} = e_1(1\text{-}\exp(-r_1 t)) + e_2(1\text{-}\exp(-r_2 t)) \qquad 3.4$$

This equation was used to curve fit the data using a least-squares fitting process in KaleidaGraph™.

CHAPTER 4
SOLUTIONIZATION OF CARBIDE PRECIPITATES IN TI-47AL-2NB-2MN-0.08VOL%TIB$_2$ + 0.1WT%C

4.1 Introduction

The addition of various alloying elements and their effect on phase stability and mechanical properties has improved the balance of various mechanical properties in near-γ TiAl alloys, particularly creep resistance and ductility [4]. Certain near gamma alloys, which have displayed exceptional strength at elevated temperatures, have been developed using the XD™ process. Cast alloys produced by this method contain a needle-like TiB and a blocky TiB_2 particulate phase dispersed throughout the alloy [5]. The addition of carbon to XD™ gamma alloys has shown to improve the creep resistance of the alloy [6]. The carbon improves the strength of the alloy by carbide formation. The orientation relationship of the carbides with its host matrix has been shown to be [7-10]

$$[100]_{ppt}//[100]_{TiAl}, [001]_{ppt}//[001]_{TiAl}.$$

The precipitates that form have a perovskite and H-phase structure and have been identified as Ti_3AlC and Ti_2AlC with a spherical and rod-like morphology [11]. The type of precipitate that forms has been shown to depend on the heat treatment temperature and time selected for the aging process [65.]

One of the objectives of the XD™ alloy development program, funded by the Howmet Research Corporation, (Whitehall, MI, U.S.A), is to determine a cost effective heat treatment process that will utilize the maximum strengthening effects from the carbide precipitates. However, before classical aging studies can be conducted, the first step in the program is to solutionize the carbides formed during cooling from the HIP (Hot Isostatic Pressing) process.

This chapter will focus on two primary goals of the alloy development program. One, to characterize the precipitates in an as-HIPed near-gamma titanium aluminide alloy with a nominal composition of Ti-47Al-2Nb-2Mn-0.8vol% TiB_2 + 0.07at% C by shape, size, and distribution within its host matrix. Secondly, to determine if the solutionizing heat treatments did in fact solutionize the carbide precipitates. Scanning electron microscopy (SEM) and transmission electron microscopy (TEM), using selected area diffraction techniques coupled with bright and dark field imaging, will be used to obtain the above objectives. Computer simulations of diffraction patterns of different high and low index zones were used to aid in the determination of the orientations of the phases examined.

4.2 Results and Discussion

The solutionizing temperatures that were investigated and the corresponding precipitate sizes and standard deviations were listed in Table 6. Secondary electron images from solutionizing attempts at 1090°C (~2000°F) for 1hr and 1230°C (~2250°F) for 2hrs are shown in Figure 16. The majority of the carbides observed were spherical in shape. The sizes of the precipitates decreased with increasing solution heat treatment temperature and they were inhomogeneously distributed throughout the microstructure as shown in Figure 16.

Table 6 Times and temperatures used to determine solutionizing temperature of carbon in alloys investigated. Observations of the microstructure were made using a Scanning Electron Microscope and Transmission Electron Microscopy. Average diameter (standard deviation) in nm

Solutionizing Temperature	Time (hrs)	Observations of microstructure after solutionizing heat treatment.
1090°C (~2000°F)	1	Precipitates still visible, non-uniformly distributed throughout microstructure with average size of 53.8nm (37.5nm)
1150°C (~2100°F)	2	Precipitates visible but getting smaller in size, non-uniformly distributed throughout microstructure with average size of 34.5nm (16.4nm)
1230°C (~2250°F)	2, 4	Precipitates less visible and smaller in size with an average of 21.5nm for 2hr attempt and 11nm for 4hr anneal (7.9nm, 5.9nm)
1300°C (~2370°F)	8	Supersaturated solution obtained at 8-hour heat treatment.
1350°C (~2460°F)	8	Supersaturated solution obtained at 8-hour heat treatment.

There was no apparent relationship between the distribution of carbides in a grain and the types of grains surrounding the grains containing the precipitates. With higher attempted solution temperature, it became increasingly difficult to view the precipitates using SEM to infer if they had been solutionized. Therefore, TEM was used to further characterize the microstructures. The as-HIPed and solutionized foils from the 1300°C (~2370°F) – 8hr solution treatment exhibited dissimilar microstructures. The as-HIPed samples displayed a nearly lamellar microstructure having smaller volume fractions of equiaxed γ-TiAl grain clusters. The solutionized microstructure was also nearly lamellar with smaller γ grains and larger α_2/γ lamellar colonies with needle-like TiB and blocky TiB_2 particulates dispersed randomly throughout the microstructure. Precipitates ranging from 60-150nm were also observed in the as-HIPed samples in the equiaxed γ grains and in the γ/α_2 lamellae interfaces. Figure 17 shows the phases present in the as-HIPed foils examined.

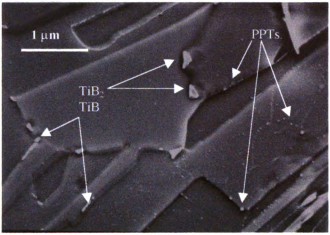

(a)

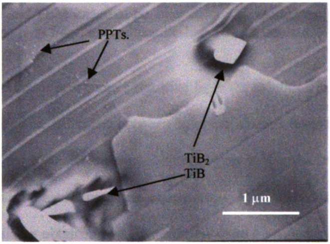

(b)

Figure 16 Secondary electron images of attempted solutionizing temperatures of (a) 1090°C (~2000°F) for 1hr, and (b) 1230°C (~2250°F) for 2hrs. Both needle-like TiB and blocky TiB_2 can be seen the micrographs.

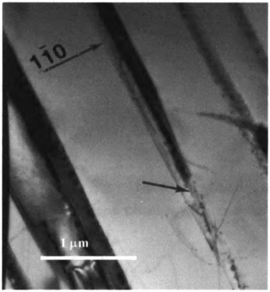

Figure 17. Microstructure of as-HIPed specimen showing the particular phases in the alloy. Bright Field TEM image of lamellar colony showing precipitate phase along α_2/γ interface and needle-like TiB particulate.

The distribution of precipitates resulting from the solutionizing attempts is shown in Figure 18. The difference between aging parameters investigated in this study versus Tian and Nemoto and Appel and Wagner is that the length of time held at the solution temperature was shortened. This was done to see if solutionization could be obtained at a time suitable from a production standpoint. The multimodal distribution of precipitate sizes in the as-HIPed condition was observed in all of the solution attempts with the size distribution of precipitates decreasing with increasing solution parameters.

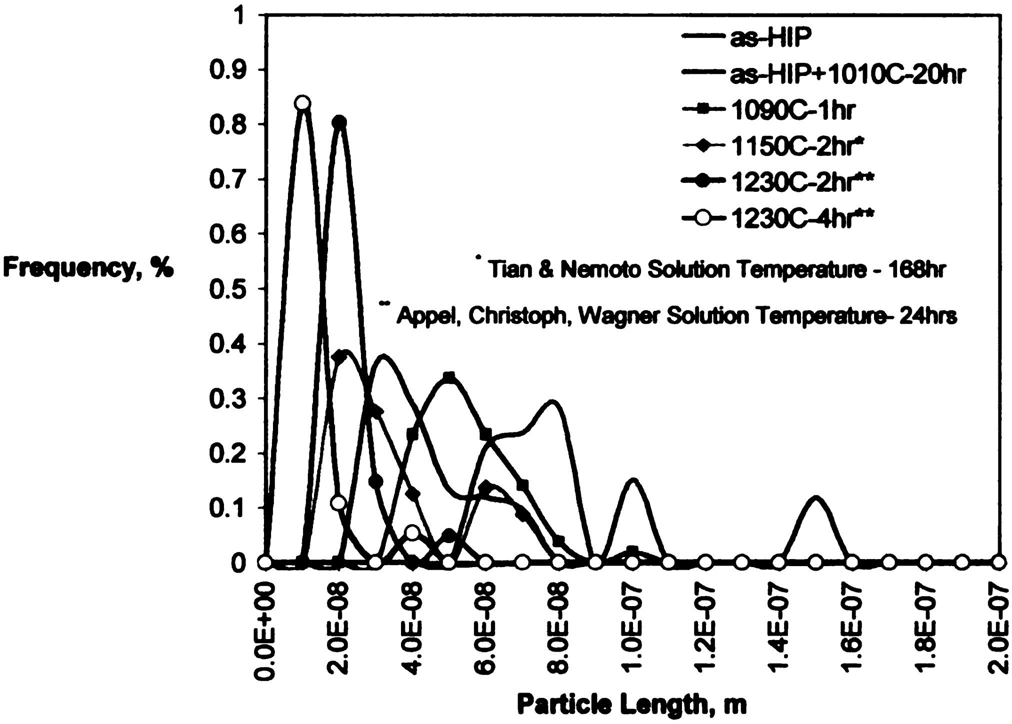

Figure 18 Distributions of precipitates resulting from solutionization heat treatments.

To determine that the particles observed were carbide precipitates, selected area diffraction (SAD) was used to verify the crystallographic relationship of the precipitates with the gamma matrix. The foils were tilted and rotated to a known zone axis and accompanying bright field (BF) images were taken. The extra spots that appear in the diffraction pattern in Figure 19 are from the precipitates and correspond to forbidden reflections for the ordered face-centered tetragonal γ-TiAl phase.

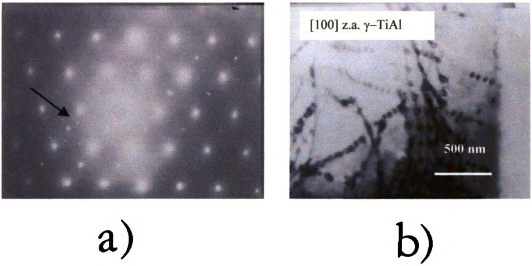

Figure 19 (a) SADP of (b) BF image of an equiaxed γ-TiAl region in the as-HIPed condition. Note extra spots from the precipitate phase, which correspond to forbidden reflections for TiAl.

Energy Dispersive X-ray (EDX) analysis was also performed to help in identifying phases present. As in the SEM images, examination of the γ-TiAl regions in the as-HIPed foils revealed heterogeneous distributions of precipitates from grain to grain. The distribution of precipitates at the α_2/γ interfaces in the lamellar colonies also differed from lath to lath within the colonies examined. These findings differ from those recorded in a previous study conducted by Chen, Beaven, and Wagner in which very fine homogeneously distributed carbide precipitates were observed only within the γ-TiAl grains [10].

The microstructure of the solutionized foils was primarily composed of large lamellar colonies with small-interspersed equiaxed γ grains and randomly dispersed boride particulates. The solutionized samples were completely void of carbide precipitates. To verify this, BF and SAD images were taken in the orientation that the precipitates have been shown to have with the gamma matrix. Figure 20 is a BF image showing a gamma grain, taken from the 1300°C-8hr solution attempt, without any precipitation visible, and its corresponding SAD.

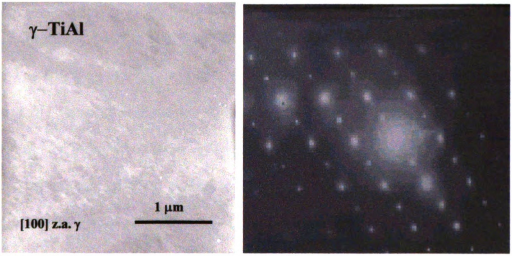

(a) (b)

Figure 20 Microstructure of solutionized sample. (a) Equiaxed gamma grain in 1300°C-8hr did not contain any precipitates (60,000X). This was confirmed by taking (b) a SAD pattern of area that was void of precipitate in orientation that precipitates are observed in this alloy. Note no extra spots are observed.

4.4 Summary

Carbon additions to near-gamma XD™ titanium aluminides result in the formation of precipitates in the alloy when cooled from the HIP treatment. These precipitates create extra spots in the diffraction pattern that correspond to the forbidden reflections in the ordered f.c.t γ-TiAl phase. The precipitates were dispersed randomly throughout the microstructure compared to previous investigations. In order to produce a supersaturated solution of carbon in near-γ alloys, various solution heat treatments were investigated. After a stabilizing heat treatment of 1300°C (~2370°F) for 8hrs, the precipitates observed in the as-HIPed condition were completely dissolved into the host material.

CHAPTER 5
THE INFLUENCE OF AGE HARDENING ON PRIMARY CREEP RESISTANCE IN A NEAR-GAMMA 47XD™ TITANIUM ALUMINIDE WITH 0.078 WT% CARBON

5.1 Introduction

Extensive research efforts have provided an understanding of the effects that heat treatments and changes in composition have on the properties of TiAl-based alloys [7]. The addition of carbon to near gamma alloys has been shown to be an effective alloying element that increases the creep resistance when in the form of precipitates [6,7,14].

The carbide precipitates have been observed to form in the single-phase γ-TiAl, on dislocations, and at the α_2 / γ interface with the orientation relationship of $[100]_{ppt}//[100]_{TiAl}$, $[001]_{ppt}//[001]_{TiAl}$ [7,69,82]. The precipitates have been found to range from 5-100nm in length and have diameters 6-8nm with a spherical and rod-like morphology. These precipitates have been identified as Ti_3AlC and Ti_2AlC [9]. The morphology of the precipitates is related to the aging temperature and time [65]. At lower temperatures spherical precipitates are formed with the perovskite structure while at higher aging temperatures rod-like precipitates are observed with the H-phase structure [69].

Certain XD™ alloys, which contain TiB and TiB_2 particulates dispersed throughout the alloy, produced at the Howmet Research Corporation (Whitehall, MI, U.S.A) contain carbon as an interstitial alloying element. This study focuses on the behavior of a XD™ alloy containing carbon and the role of carbon in precipitation hardening. This investigation describes the development of cost effective heat treatment processes that optimize the strengthening effect from the carbide precipitates using classical age-hardening studies. Room temperature tensile tests and high temperature primary creep experiments are used to evaluate the strengthening effects of the carbide precipitates. Transmission electron microscopy (TEM) was used to characterize the precipitates by shape, size, and distribution within its host phase. The procedures followed to generate the data presented in this chapter were described in Chapter 3.

5.2 Results

Several test bars were exposed to a solution heat treatment to obtain a homogenous solid solution and then quenched to room temperature to create a supersaturated condition. This solution temperature was chosen from solutionizing experiments conducted by the Howmet Research Corporation (Whitehall, MI, U.S.A) which was discussed in the previous chapter. The test bars were then separated into the groups outlined by the test matrix in Table 7 for evaluation. After aging, the specimens were cooled to room temperature by quenching in oil.

5.2.1 Microstructures

The microstructures produced from the heat treatment-aging schemes listed in Table 7 consisted of a duplex microstructure with approximately 30-50 pct lamellar content, and nearly lamellar microstructures with lamellar contents of approximately 75 pct. Backscatter electron (BSE) images of these microstructures are shown in Figure 21. The equiaxed gamma grains were dispersed randomly throughout the microstructure in small clusters surrounded by larger lamellar colonies. The average grain sizes of the constituent phases obtained from the selected heat treatments along with their volume fractions are listed in Table 7.

The equiaxed gamma grain size and the lamellar colony size increased with increasing aging time at a given aging temperature over all of the temperatures investigated. The largest increase in grain size was observed in the solutionized specimen that was aged at 1100°C for 40 hrs. The equiaxed gamma grain size increased from 39 to 64 microns between 2 and 40 hours. TiB_2 and TiB particles were randomly distributed in the aged specimens but were more homogeneously distributed in the as-HIPed and as-HIPed + 1010°C°F heat-treated microstructures.

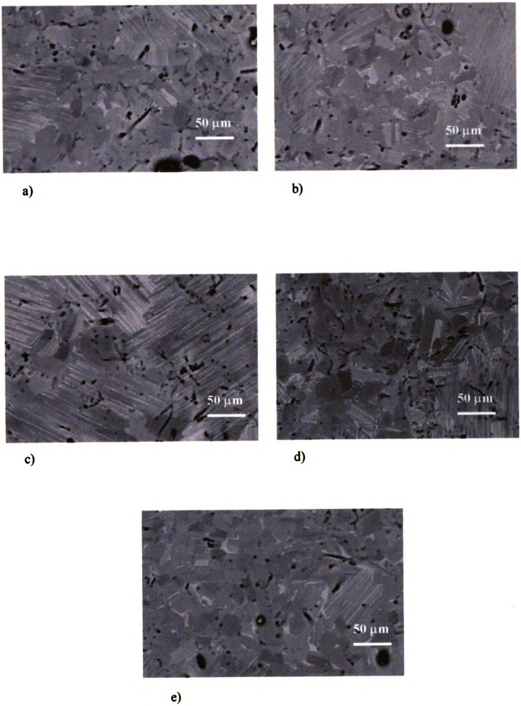
50 µm
50 µm
a)
b)
50 µm
50 µm
c)
d)
50 µm
e)

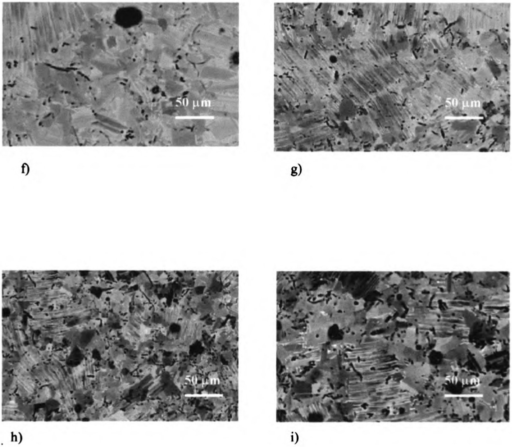

f) g)

h) i)

Figure 21 Back scattered electron (BSE) images of representative microstructures from the different heat treatment/aging conditions investigated. The black "spots" that appear in the microstructures are remnant locations of TiB and TiB_2 that were removed during sample preparation (a) as-HIPed, (b) as-HIPed + 1010°C-20hr, (c) 1300°C-8hr "Solution" (d) 950°C –2hr, (e) 950°C-40hr, (f) 1000°C-2hr, (g) 1000°C-40hr, (h) 1100°C-2hr, and (i) 1100°C-40hr.

Table 7 Average grain sizes from selective heat treatments along with volume fractions and microstructures (lam = lamellar).

2 hour				
ID	γ%	γ-grain size, μm	lam %	lam grain size, μm
as-HIPed	22	52	79	115
1300°C-8hr (Soln)	18	31	82	119
Soln+950°C-2hr	50	34	50	105
Soln+1000°C-2hr	45	54	55	111
Soln+1100°C-2hr	48	39	52	137

40 hour				
ID	γ%	γ-grain size, μm	lam %	lam grain size, μm
as-HIPed+1010°C-20hr	47	73	53	100
Soln+950°C-40hr	61	48	39	119
Soln+1000°C-40hr	25	54	75	129
Soln+1100°C-40hr	37	64	63	164

The precipitation of carbides from the aging schemes given in Table 5 were characterized with TEM. The shape, size, and distribution of carbide precipitates varied with aging for the times and temperatures investigated. Table 8 lists the average size of precipitates and standard deviation, their shape and observed spatial distribution with each heat treatment and aging time investigated. Figure 22a-d are representative microstructures showing variations in precipitate size, morphology, and distribution with heat treatment temperature and aging time. At lower aging temperatures small clusters of spherical precipitates were observed in equiaxed gamma grains. This was confirmed by tilting the foils relative to the beam axis and observing their shape. Figure 23 shows the distribution of precipitates for the different heat treatment and aging schemes evaluated. There is a continuous increase in precipitate size with increasing temperature and time. Precipitates were also identified in lamellar colonies, shown in Figure 24, where in previous studies they were not observed [65,69]. Roughly 80 pct of the grains examined in the lower aging temperature range (<1000°C) had precipitates which ranged in size from 3 – 33 nm.

Table 8 The effect of heat treatment temperature and aging time on the size, morphology, and distribution of precipitates. A minimum of 10 grains was observed in each condition. * Denotes solution heat treat at 1300°C for 8hr prior to age.

	2 Hour	**40 Hour**
	Morphology/ Distribution Avg. size nm (stdev)	Morphology/ Distribution Avg. size nm (stdev)
950°C *	Spherical precipitates with 80% of γ grains had precipitates. Precipitates also observed in 30% of lamellar grains 14.3 (7.1)	Spherical precipitates with 75% of γ grains had precipitates. Precipitates also observed in 30% of lamellar grains 19.4 (8.3)
1000°C *	Spherical and Rod-like precipitates observed in 60% of γ. Precipitates also observed in 10% lamellar grains. 19.0 (11.4)	Rod-like precipitates observed in less than 40% of γ grains. 26.6 (11.1)
1100°C *	Spherical and Rod-like precipitates observed in less than 30% of γ grains. 26.1 (12.7)	Spherical and Rod-like precipitates observed in less than 30% of γ grains. 31.1 (16.8)
As-HIPed	Spherical precipitates in ~50% of γ grains. 83.5 (27.5)	-
As-HIPed +1010°C-20hr	Spherical precipitates in ~50% of γ grains. 40.7 (13.8)	-

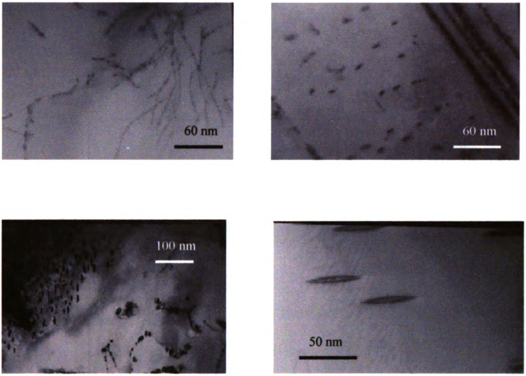

Figure 22 TEM images showing how aging affected microstructure. The size of precipitates varied with heat treatment and aging time for (a) 950°C-2hr, (b) 1000°C-2hr, (c) 1100°C-40hr (d) 1100°C-40hr close up of precipitate.

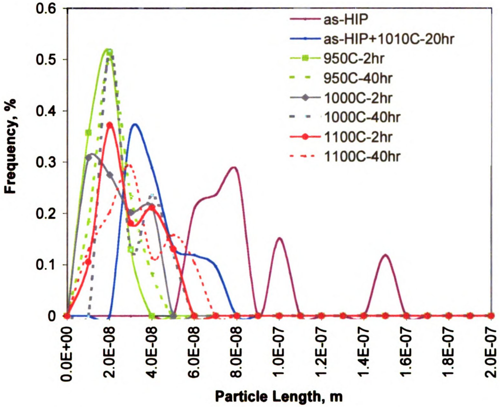

Figure 23 Ditributon of average precipitate diameter for the different heat treatment and aging schemes studied.

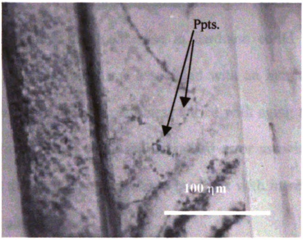

Figure 24 Precipitation of carbides in lamellar grains.

As the heat treatment temperature increased along with aging time, the morphology of the precipitates changed along with their distributions. At higher aging temperatures the morphology of the precipitates changed from spherical to rod-like as shown in Figure 22b-d. This was confirmed by tilting the foils relative to the beam axis and observing the appearance of the precipitates. At the higher aging times and temperatures the precipitates became heterogeneously distributed. Precipitation in lamellar colonies was less frequently observed at the higher heat treatment temperature and longer aging times.

5.2.2 Room Temperature Properties

The room temperature microhardness of each heat treatment was evaluated to determine if an increase in hardness could be identified with a specific aging heat treatment and associated with an increase in yield strength. Figure 25 shows how the microhardness varied with aging time and temperature for the alloy investigated along with standard error associated with each aging parameter. In this figure an increase in hardness with increasing aging time and temperature is observed.

Figure 26 shows how heat treatment and aging affected the yield strength and ductility of the alloy investigated. A decrease in yield strength was observed when giving the as-HIPed specimens a normalizing heat treatment of 1010°C for 20 hrs. The yield strength of the samples with carbon in solution was lower than the as-HIPed condition where the carbon is still in the form of large precipitates. Aging the solutionized samples increased the yield strength both with increasing aging time and increasing temperature. The room temperature ductility increased for the as-HIPed specimens when subject to the normalizing heat treatment of 1010°C for 20 hrs. The ductility in the solutionized specimens also decreased compared to the as-HIPed condition. The ductility of the aged specimens increased with aging time and temperature. These results follow fundamental strength-ductility relationships which states that as the strength increases there is a concomitant decrease in ductility.

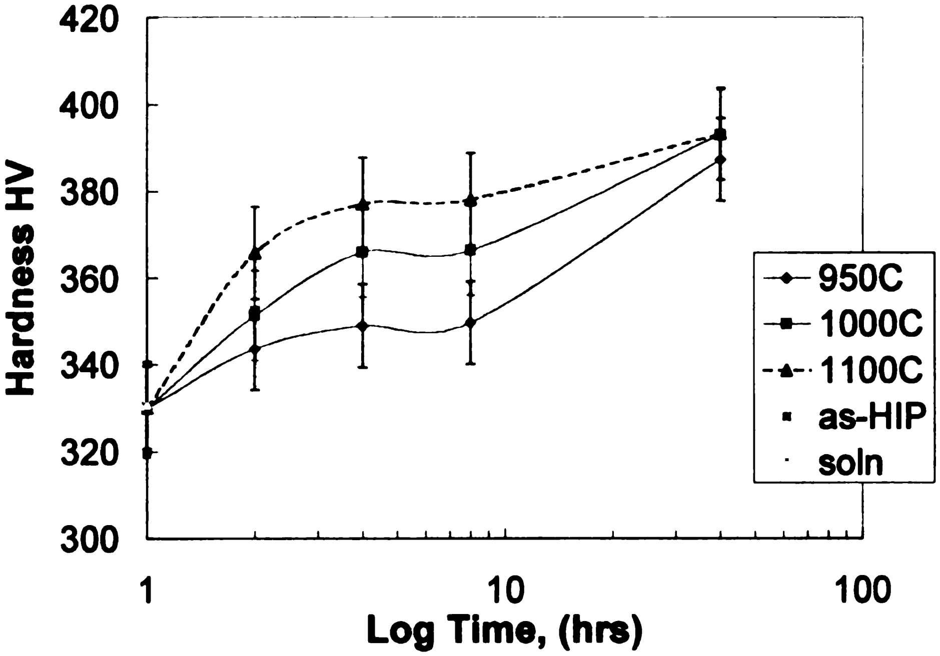

Figure 25 Classical age-hardening curve. As the aging temperature and time increased the hardness also increased.

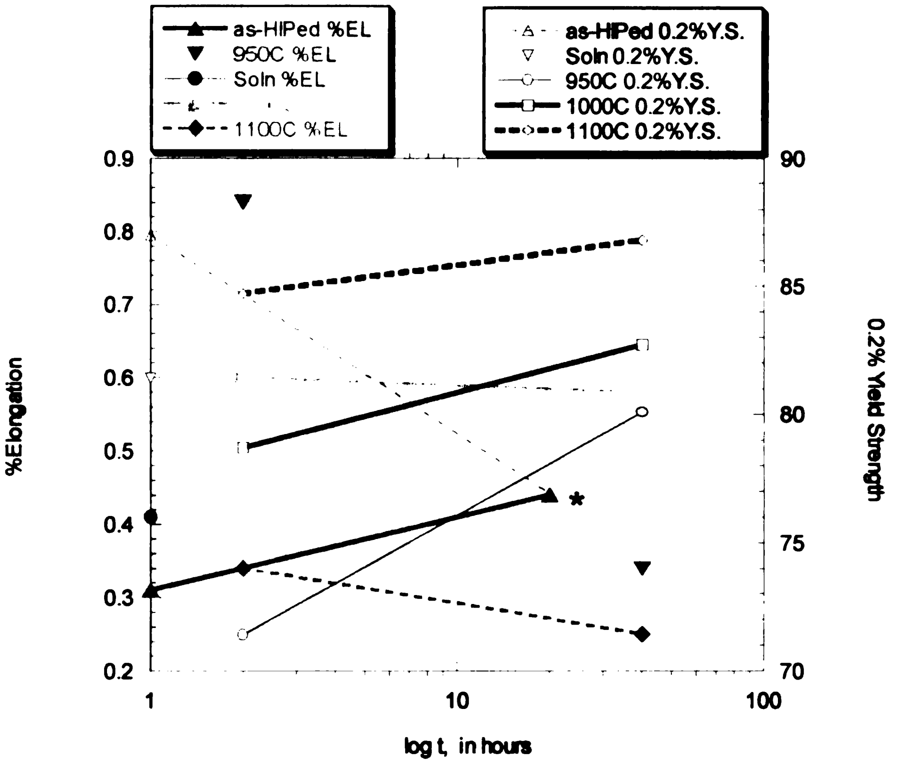

Figure 26 The effect of aging on yield strength and ductility. With an increase in yield strength a decrease in ductility was observed with increasing aging temperature and time. (* Denotes 20hr heat treatment at 1010°C)

5.2.3 Creep Resistance

The effect of aging on the time to 0.5% creep strain for the different heat treatment temperatures and aging times is shown in Figure 27. A reduction in the time to 0.5% creep strain was observed for the as-HIPed specimen when given a normalizing heat treatment at 1010°C for 20 hrs. The as-HIPed microstructure also exhibited better primary creep resistance compared to the solution heat treated microstructure. The effect of aging on the primary creep resistance of the aged specimens was more dramatic than on the as-HIPed and normalized as-HIPed samples. Aging for 2hrs at the 950°C, 1000°C, and 1100°C showed primary creep resistance about twice as good as aging for 40hrs.

The average size of the precipitates is plotted along with times to 0.5% creep strain in Figure 28. Heat treating the as-HIPed microstructure caused a decrease in the average size of the precipitates and a decrease in creep resistance. As aging time and temperature increased the average precipitate size increased, and the times to 0.5% creep strain showed an increasing trend with aging temperature.

In Figure 29 the time to 0.5% creep strain is plotted against lamellar volume fraction, which was different for the two specimens tested at each condition. As the heat treatment and aging times increased there was an observed increase in the volume percent of lamellar colonies and a corresponding increase in the primary creep resistance.

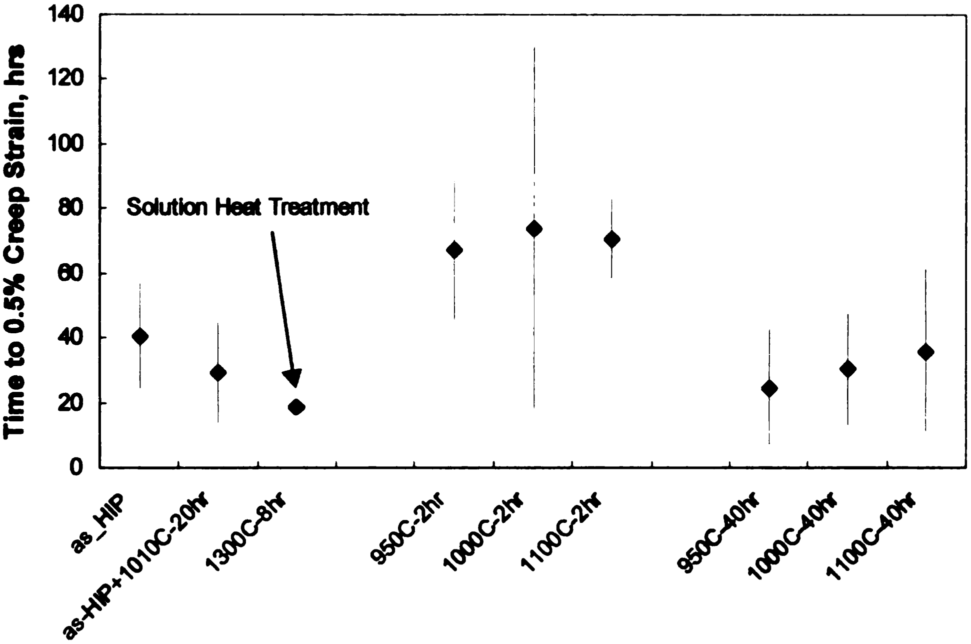

Figure 27 Time to 0.5% creep strain with respect to heat treatment.

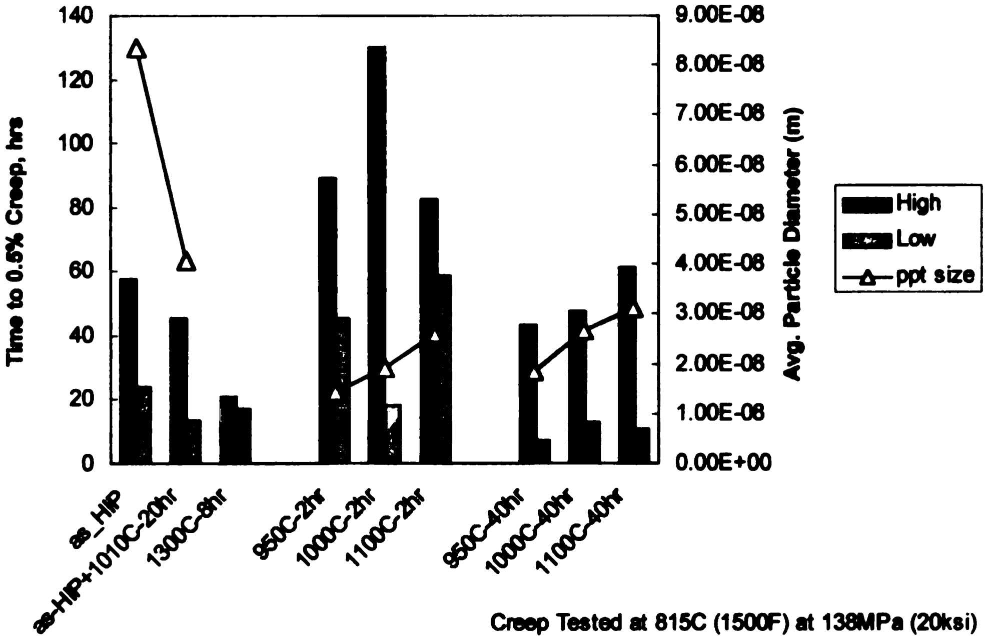

Figure 28 Time to 0.5% creep strain with respect to precipitate size.

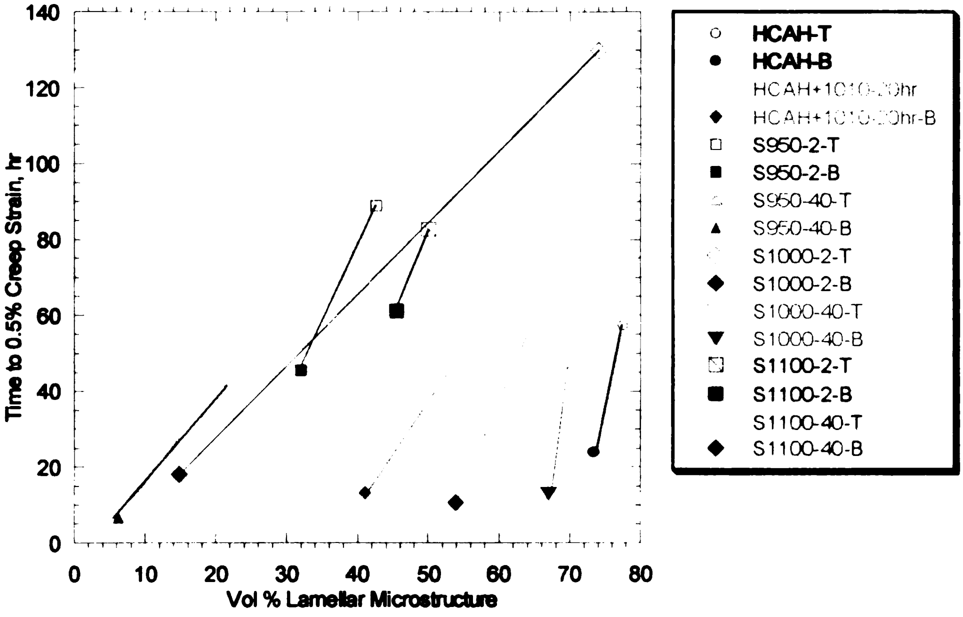

Figure 29 Times to 0.5% creep strain with respect to vol% lamellar grains. Creep Resistance increases with increasing volume fraction lamellar grains.

5.4 Discussion

The results given in this study will be examined by first looking at how precipitation contributed to the room temperature properties by comparing mechanical test data and microstructure followed by a similar comparison of creep resistance and microstructure at elevated temperatures.

The hardness of a material is the resistance of the material to plastically deform so it is also an estimator of the yield strength. As a result of aging, the hardness increased along with the yield strength of the alloy. In Figure 25, as the aging temperature and time were increased, an increase in hardness was recorded. Aging theory tells us that if the heat treatment temperature is too high or the aging temperature is too long an overaged condition may result. This phenomena was not observed in this study where after aging for 40 hours the hardness was still increasing for each aging temperature evaluated. In Figure 26 the yield strength and ductility with respect to aging is illustrated. Both properties behaved according to basic metallurgical principles in that they were inversely proportional to one another over the aging time and temperatures evaluated. Thus it appears that classical aging behavior is observed.

The aging behavior of the as-HIPed condition differed considerably from the solutionized and aged specimens. From Figure 25 the effect of aging the as-HIPed specimen seemed to indicate that the as-HIPed microstructure might exist in the overaged condition. Although this can not be shown over a range of time on the aging curve, one may infer this because the hardness of the as-HIPed material was lower than the hardness of the solutionized condition. This inference is supported by the fact that the yield strength of the as-HIPed microstructure decreased with heat treating at 1010°C for 20hrs. However, by looking at the standard error of the hardness at each aging parameter, the change in hardness becomes less significant. Noting this and the fact that some of the data presented in Figure 26 are averages, while others are single data points, seems to indicate that classical laboratory techniques to infer aging characteristics cannot be used. To gain a better understanding of the aging behavior of this alloy, the creep resistance and precipitate size, morphology, and distribution of precipitates in the as-HIPed and solutionized conditions were compared to the aged specimens.

The times required for the development of 0.5% creep strain were plotted against heat treatment and aging time in Figure 27. From this figure it is clear that aging after solutionization affects the primary creep resistance in this alloy. The greatest creep resistance was achieved with the 1000°C age for 2 hours. In this figure the creep resistance at each aging temperature was notably larger for the 2-hour age versus the 40-hour aging time.

To explain why a difference was observed, the microstructures of each aging scheme were examined. An explanation for the difference observed between the high and low times are given in the next chapter. In Figure 28 the relationship between the time to 0.5% creep strain and average precipitate size is shown. Aging theory tells us volume fraction, and distribution of strengthening precipitates is of importance for property control of age hardenable alloys. In the microstructures shown in Figure 22 a range of precipitate sizes can be seen. The distributions shown in Figure 23 suggests that aging for extended periods of time and at higher temperatures produces a wider range of precipitate sizes. From Table 9, the 1000°C – 2hr aging scheme, which had the longest time to 0.5% creep strain, did not have the smallest size of precipitates. However, looking at the distribution of precipitates in Figure 23 we see a bimodal distribution of precipitates for the 1000°C-2hr aging scheme with the largest fraction having an average diameter of 10nm. The only other heat treatment that had an average time to 0.5% creep strain that was close to the 1000°C-2hr was the 1100°C-2hr aging scheme. Again a bimodal distribution is observed with the largest fraction of precipitates having a diameter of 20nm. Although the 950°C aging temperature had similar average size precipitates, the distribution of precipitate size was different and the corresponding creep resistance was poorer. As aging time increased, precipitate size increased and there was an average decrease in time to 0.5% creep strain. The observed decrease in creep resistance between the 2 and 40 hour aging schemes may be related to this increase in precipitate size, and a consequent increase in spacing, which is difficult to determine due to the heterogeneous distribution. It is worth noting that the morphology and spatial distributions of precipitates, as well as the percent lamellar volume fraction, differed with each aging scheme evaluated.

At lower temperatures and shorter aging times more spherical precipitates were observed than the rod-like particles seen in other studies [7,65]. It is also important to note that precipitation was observed at these shorter aging times in contrast to other studies which did not see precipitation until after aging at least 10-15 hours at the same temperatures investigated here [69].

As the aging temperature and times increased, more rod-like precipitates became visible. The distribution of precipitates at lower aging temperatures were homogeneously distributed in equiaxed gamma grains while at higher temperatures and extended aging times yielded heterogeneously distributed precipitates primarily along grain boundaries, dislocations, and lamellar grains. Looking at the precipitate distributions and volume fractions of microconstituents helps explain the observed relationship between aging time and temperature and time to 0.5% creep strain.

It is well known that the creep resistance increases with increasing volume fraction of lamellar grains in near-γ alloys. In Figure 29 a higher volume fraction of lamellar grains corresponded with an improvement in primary creep resistance. Again a difference between the 2 and 40 hour aging times is evident. The most prominent increase was observed in the 1000°C heat treatment between the 2 and 40 hour age time. This result suggests that the volume fraction of lamellar colonies is also contributing to the increase in primary creep resistance. The difference between top and bottom creep rates is discussed in the following chapter.

5.5 Summary

The classical aging study conducted in this experiment yielded results that show by judicious selection of heat treatment temperature and aging time that the mechanical properties of this alloy can be enhanced. The magnitude of precipitation strengthening relative to that of solid solution strengthening is large. Classical aging theory tells us that the distribution and size of the strengthening precipitates significantly affects the attainable strength and can be manipulated by controlled aging temperatures and times. However, based on the above results there was no clear aging scheme that beyond doubt seemed to optimize the strengthening effects of the carbide precipitates. Heat treating at 1000°C and aging for 2 hours shows to be the most promising aging scheme when looking at times to 0.5% creep. Despite the small variation in the average size of precipitate, it is clear that the near gamma TiAl alloy Ti-47Al-2Mn-2Nb + 0.08vol%TiB_2 + 0.07wt% C is age hardenable. Further investigation of longer aging times and the effect on mechanical properties along with the deformation mechanisms involving precipitate – dislocation interactions will aid in clarifying the optimal aging scheme.

CHAPTER 6

THE EFFECT OF HIPING ON REMOVAL OF CENTERLINE POROSITY AND FORMATION OF EQUIAXED GAMMA GRAINS ON PRIMARY CREEP RESISTANCE IN NEAR-GAMMA XD™ TITANIUM ALUMINIDES

6.1 Introduction

It is well known that in the as-cast state, gamma alloys have very poor ductility due to the micro and macro porosity retained from the casting process. This porosity exists primarily in the center of castings and is therefore referred to as centerline porosity. Thus the as-cast components require Hot Isostatic Pressing to close the porosity. Pore closure promotes the formation of equiaxed gamma grains resulting in a microstructure that varies from centerline to edge [90,91]. Mold design and mold filling phenomena affect the amount of porosity that is retained in the casting.

The extent of the formation of equiaxed gamma grains from HIPing, and its effect on mechanical properties has not been adequately explored. This is an important issue that has gained little attention and with further insight may be able to elucidate the variability that is seen in mechanical test data [6]. One possible explanation for the observed variability may be that a relationship exists between specimen geometry, test specimen location within a casting and the extent of equiaxed gamma grains formed after HIPing.

It has been reported in numerous investigations that creep resistance in near-gamma alloys is very sensitive to microstructure [12,65,69]. The fully lamellar microstructure has better creep resistance compared to equiaxed gamma and duplex microstructure [65]. In this chapter, the variability in primary creep resistance (time to 0.5% creep strain) seen in the data presented in the previous chapter is examined. To determine the role of equiaxed gamma grain formation in the HIPed material and its relationship with variability in creep resistance, microstructure and creep resistance of specimens machined from the top and bottom of cast test bars will be compared.

6.2 Results

6.2.1 45XD™ Carrot and Inverted Carrot Specimens

Macro images showing the effects of centerline shrink in both inverted and carrot specimens are shown in Figure 30. Detailed microstructures of the carrot and inverted carrot specimens are shown in Figures 31 and 32. The inverted carrot test bars had considerably more equiaxed gamma grains than in the carrot specimens. The volume fraction of equiaxed gamma grains decreased from center to edge and increased from top to bottom in the inverted carrot microstructures. In the bottom portion of the inverted carrot specimen the gamma grains were randomly distributed among lamellar grains. Towards the middle of the inverted carrot bar a large cluster consisting of equiaxed gamma grains was observed as shown in Figure 32b. The carrot specimen also exhibited similar microstructural characteristics with large clusters of equiaxed gamma grains at the center of the casting.

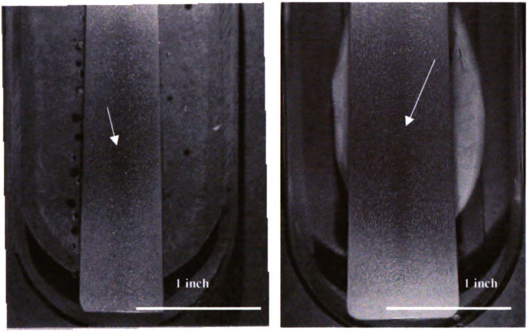

(a) (b)

Figure 30 Cross section views of (a) carrot and (b) inverted carrot specimens showing centerline shrink.

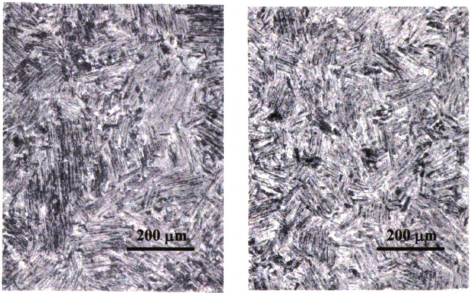

a) b)

Figure 31 Characteristic microstructures of the (a) carrot specimen and (b) inverted carrot specimen taken from the top of the specimens in the centerline shrink area.

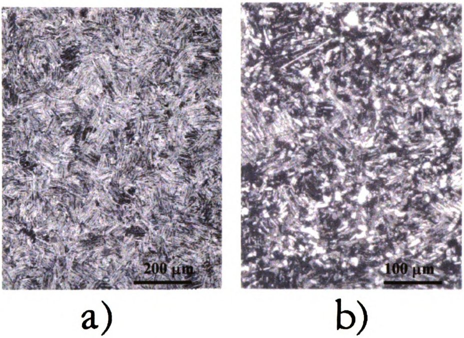

Figure 32 Microstructures of centerline shrink area taken in the middle of the (a) carrot and (b) inverted carrot test bars. Note the difference in grain size and volume fraction of equiaxed gamma grains and lamellar colonies.

6.2.2 47XD™ Carbon Alloys

Similar microstructural features that were observed in the 45XD™ alloy were also seen in the 47XD™ carbon containing alloys. Figure 33 shows BSE images that illustrate the change in average grain size and volume fraction in the 47XD™ specimens from top to bottom and center to edge for some of the heat treatment/aging schemes evaluated. Figure 34 shows that in all of the heat treated specimens, the equiaxed gamma grain size decreased from top to bottom in the test bars while increasing from centerline to edge in each specimen. Table 9 listed the grain size and volume fraction of microconstituents from center to edge and top to bottom in the 47XD™ alloy. The cluster size of gamma grains was larger in the bottom portion of the test bars and more frequently observed than in the top. The volume fraction of equiaxed gamma grains also increased from top to bottom and decreased from centerline to edge. In both the top and bottom specimens, the centerline areas exhibited clusters of equiaxed gamma grains surrounded by lamellar colonies. At the edge of the test specimens the equiaxed gamma grains were randomly distributed amongst lamellar colonies.

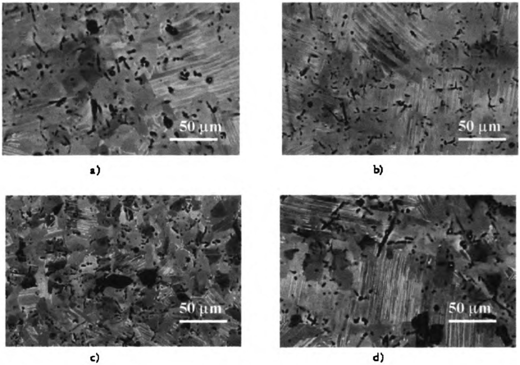

a) b) c) d)

Figure 33 Backscattered electron (BSE) images of the 47XD™ carbon alloy. Note the increase in gamma grain size from (a) top-center to (b) top-edge and increase from (c) bottom-center to (d) bottom-edge in the specimen shown. Black spots are pits created from etching away TiB and TiB_2 particles.

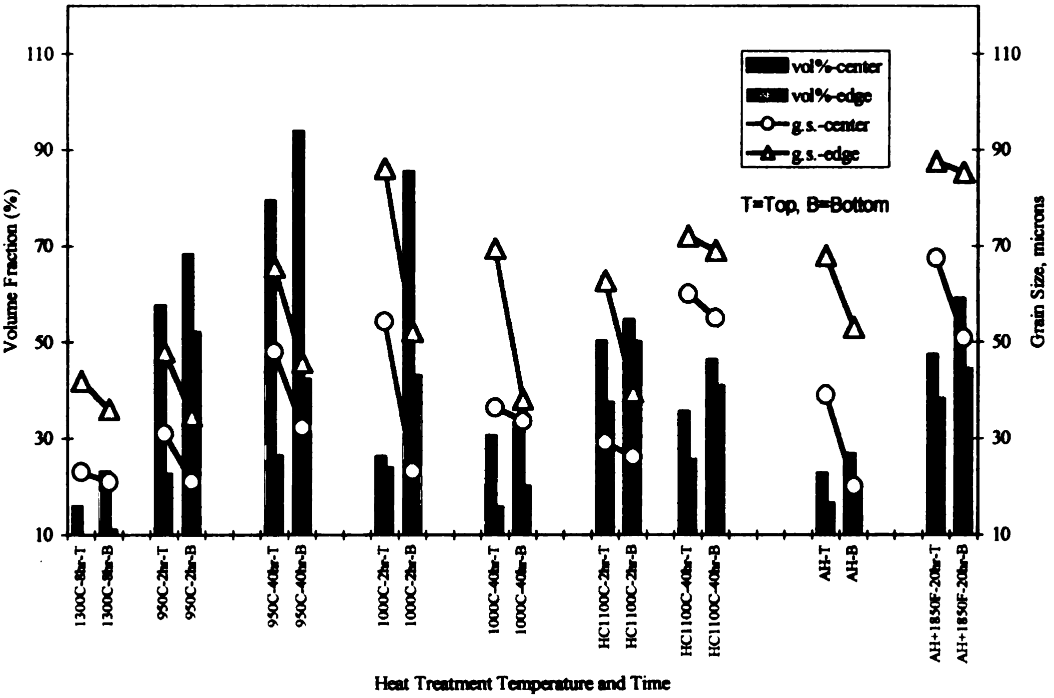

Figure 34 The variation in equiaxed gamma grain size and volume fraction from center to edge and top to bottom with heat treatment and aging time.

	TOP								
	Center					Edge			
ID	avg g.s.	avg. cluster size	avg l	%g	%l	avg g.s.	avg l	%g	%l
as-HIPed	47	267	111	22.49	77.51	68	123	20.12	79.88
as-HIPed+101C-20hr	67	298	97	47.3	52.7	88	118	38.2	61.8
1300C-8hr (Soln)	23	130	124	15.7	84.3	42	131	12.3	87.7
Soln+950C-2hr	31	217	99	57.4	42.6	48	106	22.49	77.51
Soln+950C-40hr	48	232	101	79.29	20.71	65	152	30.18	69.82
Soln+1000C-2hr	54	308	96	26.04	73.96	86	143	24	76
Soln+1000C-40hr	36	312	128	30.4	69.6	69	143	15.7	84.3
Soln+1100C-2hr	29	294	134	50.04	49.96	63	141	37.50	62.50
Soln+1100C-40hr	60	301	158	35.31	64.69	72	172	25.55	74.45

	BOTTOM								
	Center					Edge			
	avg g.s.	avg. cluster size	avg l	%g	%l	avg g.s.	avg l	%g	%l
as-HIPed	39	313	116	26.63	73.37	53	109	16.57	83.43
as-HIPed+101C-20hr	51	326	96	58.9	41.1	85	90	44.4	55.6
1300C-8hr Soln	21	147	101	23	77	36	119	19.7	80.3
Soln+950C-2hr	21	298	104	68.05	31.95	35	98	52.07	47.93
Soln+950C-40hr	32	314	107	93.75	6.25	46	118	42.19	57.81
Soln+1000C-2hr	23	368	97	85.21	14.79	52	109	43	57
Soln+1000C-40hr	34	371	129	33	67	38	116	20	80
Soln+1100C-2hr	26	389	129	54.53	45.47	40	137	50.00	50.00
Soln+1100C-40hr	55	373	159	46.16	53.84	69	168	40.78	59.22

Table 9 Grain size and volume fractions of equiaxed gamma grains and lamellar colonies from the center to the edge of the specimen and top to bottom of the test bar.

6.2.3 Creep Resistance

The influence of variation in microstructure on the creep resistance was investigated in the microstructures shown in the figures above. Creep deformation mechanisms and the influence of microstructure in TiAl alloys have been debated extensively and have shown that a number of factors contribute to the creep resistance in these alloys. In this study the effect of grain size and volume fraction of equiaxed gamma grains and lamellar colonies on creep resistance were measured to determine what relationship they may have on the variation in creep resistance. Figure 35 depicts the time to 0.5% creep strain for each heat treatment investigated. In this figure the difference in creep resistance between the top and bottom test specimen is shown. Figure 36 shows how the creep resistance varied with grain size and volume fractions of lamellar colonies.

For most of the aging schemes evaluated the specimens machined from the top portion of a test bar exhibited times to 0.5% creep strain that were twice as long as those machined from the bottom portion of the test bar. The largest difference was observed in the top specimen aged at 1000°C for 2 hours in which the time to 0.5% creep strain differed by an order of magnitude versus the bottom test bar. In all of the heat treatments investigated there was a corresponding decrease in time to 0.5% creep strain from top to bottom with decreasing volume fractions of lamellar colonies and increasing volume fractions of gamma grains.

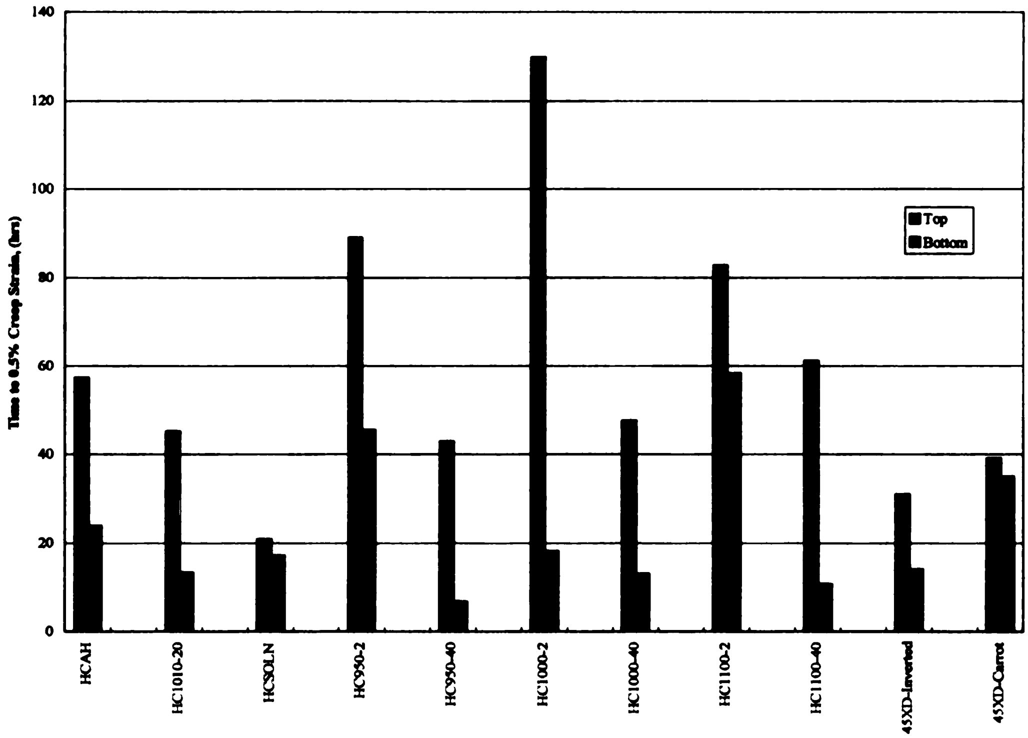

Figure 35 The variation in time to 0.5% creep strain for 47XD™ + carbon and 45XD™ inverted and carrot shaped top and bottom specimens.

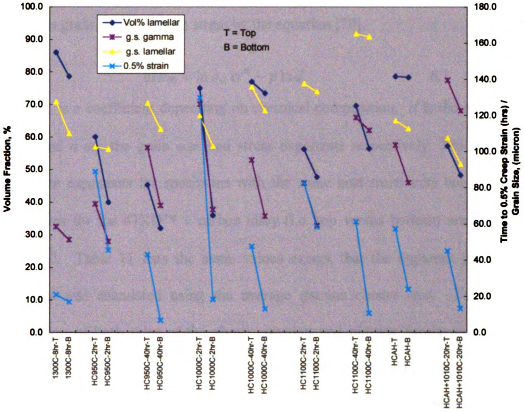

Figure 36 Times to 0.5% creep strain with grain size and volume fraction variation of microconstituents in top and bottom 47XD™ test specimens neglecting centerline to edge variations.

Based on these observations some simple analytical models were used to examine the variability in creep resistance. The rule of mixtures was applied to see if a relationship between volume % of microconstituents and creep resistance existed and creep mechanisms were explored to try to relate the observed microstructure to the variability seen in the creep data.

The minimum creep rates for near gamma alloys has been shown to be related to grain size and creep stress by the equation [70]:

$$\ln \dot{\varepsilon}_m = \ln \dot{\varepsilon}_0 \sigma^n - p \ln d \qquad 6.1$$

where ε_o is a coefficient depending on chemical composition, d is the grain size and p and n are the grain size and stress exponents respectively. The apparent grain size exponents for specimens with the same heat treatments but different grain sizes for the 47XD™ + carbon alloy (i.e. top versus bottom) are listed in Table 10. Table 11 lists the same values except that the apparent grain size exponent was calculated using the average gamma cluster size. Taking the natural log of both sides of the above equation and plotting produces a line in which the slope is equal to the grain size exponent for creep. For Nabarro-Herring controlled creep the grain size exponent should equal 1 where for Coble controlled creep the grain size exponent should range between 2 and 3.

Using the grain size, the apparent grain size exponent is not negative (i.e. the slope of the line was positive when plotting Equation 6.1) for the majority of cases, and no consistent values are found. Using the cluster size instead of the grain size produced similar results but with negative exponents appearing for most of the cases. When substituting the strain rate at 0.5% creep strain, a stronger dependence is observed. The values for the apparent grain size exponent were negative and approached values that point to specific creep mechanisms.

It has been shown that a decreasing grain size and increasing aluminum concentration can raise the minimum creep rate by at least an order of magnitude [70]. The primary creep strain-rate in the top and bottom specimens of the aged and heat treated and as-HIPed conditions are shown in Figure 37. The primary creep strain history is quite variable for the different combinations of heat treatment and microstructure.

Heat Treatment	Strain Rate at 0% Creep Strain	Strain Rate at 0.2% Creep Strain	Strain Rate at 0.4% Creep Strain	Strain rate at 0.5% Creep Strain
As-HIPed	3.8	4.5	1.5	1
As-HIPed+1010°C-20hr	-11.7	15.0	18.6	18
1300°C-8hr*	2.0	-3.6	-11.2	3
950°C-2hr	7.1	1.9	6.3	-9
950°C-40hr	3.5	3.9	0.5	4
1000°C-2hr	1.2	0.9	0.7	2
1000°C-40hr	8.5	5.1	4.0	0
1100°C-2hr	-2.7	16.1	17.8	21
1100°C-40hr	10.8	0.3	-10.9	-13

Table 10 Grain Size Dependence of Creep. The grain size exponent was determined using the average grain size of equiaxed gamma grains. *Denotes solution heat treatment.

Heat Treatment	Strain Rate at 0% Creep Strain	Strain Rate at 0.2% Creep Strain	Strain Rate at 0.4% Creep Strain	Time to 0.5% Creep Strain
As-HIPed	-11.9	-14.3	-4.6	-2
As-HIPed+1010°C-20hr	8.7	-11.1	-13.7	-14
1300°C-8hr*	-2.4	4.2	13.1	-3
950°C-2hr	-8.7	-2.3	-7.7	10
950°C-40hr	-11.4	-12.6	-1.7	-14
1000°C-2hr	-5.9	-0.1	0.0	0
1000°C-40hr	-33.0	-19.8	-15.6	-2
1100°C-2hr	2.3	-13.6	-15.1	-17
1100°C-40hr	7.7	0.2	-7.7	-9

Table 11 Grain Size Dependence of Creep. The grain size exponent was determined using the average cluster size of equiaxed gamma grains.

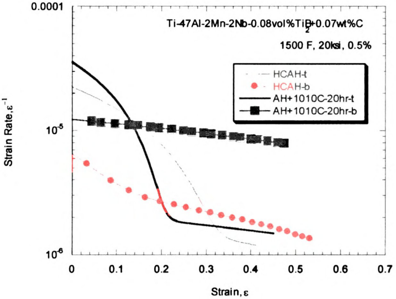

0.0001
10⁻⁵
10⁻⁶
Strain Rate, ε⁻¹
0
0.1
0.2
0.3
0.4
0.5
0.6
0.7
Strain, ε
Ti-47Al-2Mn-2Nb-0.08vol%TiB2+0.07wt%C
1500 F, 20ksi, 0.5%
HCAH-t
HCAH-b
AH+1010C-20hr-t
AH+1010C-20hr-b

(a)

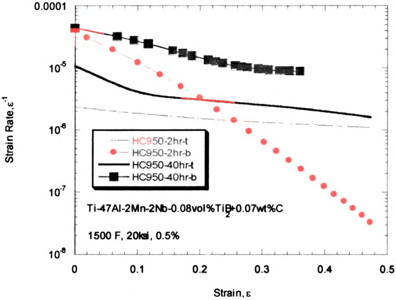

0.0001
10⁻⁵
10⁻⁶
10⁻⁷
10⁻⁸
Strain Rate, ε⁻¹
0
0.1
0.2
0.3
0.4
0.5
Strain, ε
HC950-2hr-t
HC950-2hr-b
HC950-40hr-t
HC950-40hr-b
Ti-47Al-2Mn-2Nb-0.08vol%TiB2+0.07wt%C
1500 F, 20ksi, 0.5%

(b)

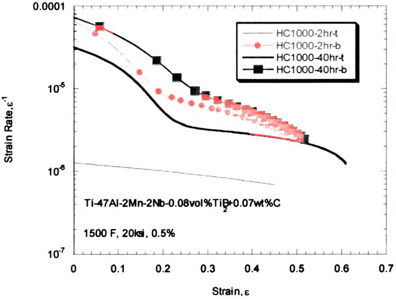

(c)

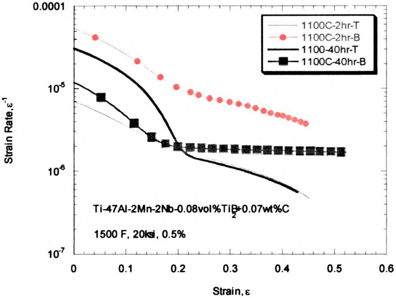

(d)

Figure 37 (a) Creep strain rate as a function of creep strain for as-HIPed and as-HIPed +1010°C-20hr, (b) 950°C, (c) 1000°C, and (d) 1100°C aging heat treatment for 2 and 40 hours. In both cases the top specimens exhibited lower strain rates than the bottom specimens.

6.3 Discussion

To explain why such variation in creep behavior exists in the data presented, a discussion of processing methods and equiaxed gamma grain formation is necessary. The extent of equiaxed gamma grain formation in the alloys examined is related to casting design and solidification fronts. The molten alloy solidified in 3 dimensions starting at the bottom of the test bars and was fed by a riser and the pour cup at the top of the casting. The top of the carrot test bar had the largest opening and contained less porosity than the inverted, which had a smaller opening at the top where molten alloy is fed to the casting. The 47XD castings had a 5/8 in. opening compared to the carrot specimens with 7/8 in opening. Both the 47XD and carrot shaped specimens contained porosity in the bottom 2/3 of the castings with the greatest amount in the inverted carrot specimens. This suggests that the amount of porosity formed during solidification is related to the geometry of the cast test bar and the effect of the solidification front on trapping porosity. The inverted carrot shape was less able to feed the lower portion of the test bar, so more porosity was trapped. After casting and HIPing the specimens, the formation of equiaxed gamma grains was more pronounced in the inverted carrot test bars, which had more porosity. From the microstructural observations more gamma grain formation occurred with more porosity retained from casting. The effect that the microconstituents have on the creep resistance requires the application of the rule of mixtures to help explain why variability is seen in the data.

From Figure 35, it can be seen that the bottom test specimens had poorer primary creep resistance than the top specimens. The results above indicate that the more equiaxed gamma grain formation in the bottom of the casting results in lower primary creep resistance for the test specimens machined from this area of the casting. In Figure 37 it is clear that two different creep mechanisms are at work during deformation with the top specimens showing better primary creep resistance than the bottom specimens. To try and make sense of the behavior shown in these figures, the rule of mixtures was explored to see if a relationship could be drawn between grain/cluster size and a specific creep mechanism.

Looking strictly at the grain size dependence of creep to explain the creep behavior did not yield results pointing to one specific creep deformation mechanism. The values for the grain size exponents listed in Tables 10 and 11 did not correspond to Coble or Nabarro-Herring creep mechanisms. It has been observed in comparing as-cast to as-HIPed radiographic transparencies that the amount of porosity in each bar of a casting varies from bar to bar. Although this data is not presented in this chapter, the fact that the amount of porosity varies from bar to bar helps explain the variation seen in the volume fractions of equiaxed gamma grains. Applying the rule of mixtures to the volume % of microconstituents did indicate a possible relationship. The data shows a decrease in primary creep resistance with increasing equiaxed gamma volume fraction in the bottom specimens and an increase in creep resistance with increasing lamellar volume fraction in the top specimens.

6.4 Summary

Combining the results from the casting geometry and microstructure along with the primary creep data a relationship can be drawn relating specimen geometry and location in a casting with primary creep resistance. The amount of porosity retained from casting is larger in the bottom portion of the test bar. HIPing the cast test material promoted the formation equiaxed gamma grain clusters in the regions containing the as-cast porosity. The resultant primary creep resistance was lower in the bottom portion of the test bar. Although there was no significant dependence of the creep rate on the grain size, the rule of mixtures suggests that the volume percent of microconstituents affects the primary creep resistance of the alloy.

CHAPTER 7
CONCLUSIONS

7.1 Aging Summary

By judicious selection of solution temperatures and heat treatments, the near gamma titanium aluminide Ti-47Al-2Nb-2Mn-0.08vol%TiB_2 + 0.1wt%C can be age hardened to increase the primary creep resistance. In this experiment, it was shown that the solutionization of carbide precipitates that form from the casting and HIP process is possible. The solution temperature found in this study was 1300°C in the $\alpha_2 + \gamma$ phase field for 8 hours. After solutionization, the classical aging study revealed that increasing the aging temperature and time increased the creep resistance of the alloy compared to the as-HIPed and as-HIPed + 1010°C heat treated condition. The size, distribution, and morphology of precipitates also changed with aging temperature and time. As the aging temperature and time increased the precipitates changed from spherical to rod-like. The distribution of precipitates from grain to grain became less homogeneous as the aging parameters were increased and the size of the precipitates increased with time and temperature.

Evaluating the effect that aging had on the primary creep resistance indicated that the optimal aging parameters for this alloy were 1000°C for 2 hours. However, comparing the shorter aging time at each temperature showed an increase in primary creep resistance versus the longer 40-hour age.

The variation that was observed in the creep data did not point to one specific creep mechanism. Coble creep mechanisms were thought to account for some of the observations, but this was insufficient when comparing the grain size exponent based upon differences in grain size from top to bottom in a test bar. Looking strictly at the rule of mixtures did seem to indicate a relationship between the volume fraction of constituents and an increase, or decrease, in primary creep resistance.

7.2 Future Work

The question that has not been answered completely is what really caused or influenced the variation in creep resistance in the test specimens machined from the same test bar. Although there is a significant amount of data showing that this alloy is age hardenable, and that variation in creep resistance might be explained by changes in microconstituents within a cast test bar, there still remains the need to further explore this phenomena. The fact that the amount of porosity in each test bar varied within a casting but existed in the same general area may be the missing link in explaining this behavior. Radiographic transparencies would shed light on this matter. The area/volume fraction of porosity in each test bar could be recorded and compared between the as-cast and as-HIPed condition. Representative volume fraction calculations from microstructural observations in these areas after HIP would then allow a conclusion to be drawn that would allow predictions to be made on the resulting creep resistance of the casting.

REFERENCES

1. Y-W. Kim, JOM. **V41**, No. 7, 1989, pp. 24-30.
2. Y-W. Kim, D.M. Dimiduk, JOM. **V43**, No. 8, 1991, pp. 40-47.
3. D.E. Larsen, Mat. Sci. and Eng. A. **A213**, 1996, pp. 128-133.
4. D.Y. Seo, T.R. Bieler, D.E. Larsen, *Structural Intermetallics*. Edited by M.V. Nathal *et al.* TMS, 1997, pp. 137-146.
5. D.E. Larsen, D.A. Wheeler, B. London, Processing and Fabrication of Advanced Materials III. Edited by V.A. Ravi *et al.* TMS, 1994, pp. 631-641.
6. D.Y. Seo, T. Everard, P.A. McQuay, T.R. Bieler, *Interstitial and Substitutional Solute Effects in Intermetallics*. Edited by I. Baker *et al.* TMS, 1998, pp. 227-244.
7. F. Appel, R. Wagner, Mat. Sci. and Eng. R. **Vol. R22**, No. 5, 1998, pp. 187-261.
8. T. Kawabata, M. Tadano, O. Izumi, *ISIJ International*, **V31**, No. 10, 1991, pp. 1161-1167.
9. W.H. Tian, M. Nemoto, *Gamma Titanium Aluminides*. Edited by Y-W. Kim *et al.* TMS, 1995, pp. 689-696.
10. S. Chen, P.A. Beaven, R. Wagner, Scripta Metall. Mater. **V26**, 1992, pp. 1205-1210.
11. W.E. Dowling Jr., W.T. Donlon, Scripta Metall. Mater. **V27**, 1992, pp. 1662-1667.
12. Y-W. Kim, JOM. V53, No. 7, 1994, pg. 30-39.
13. D.M. Dimiduk, *Gamma Titanium Aluminides*. Edited by Y-W. Kim *et al.* TMS, 1995, pp. 3-19.
14. P.A. McQuay, R. Simpkins, D.Y. Seo, T.R. Bieler, *Gamma Titanium Aluminides*. Edited by Y-W. Kim *et al*, TMS, 1999, pp. 119-126.
15. D.M. Dimiduk, P.A. McQuay, Y-W. Kim, *Gamma Titanium Aluminides*. Edited by Y-W. Kim *et al*, TMS, 1999, pg. 142.
16. S.A. Jones, R.D. Schull, A.J. McAlister, M.J. Kaufman, Scripta Metall. **V22**, 1988, pg. 1235.
17. J.A. Graves, J.H. Perepezkp, C.H. Ward, F.H. Froes, Scripta Metall. **V21**, 1987, pg. 567.

18. J.J. Valencia, C. McCullough, C.G. Levi, R. Mehrabian, Scripta Metall. **V21**, 1987, pg. 1141.

19. C. McCullough, J.J. Valencia, H. Mateos, C.G. Levi, R. Mehrabian, K.A. Rhyne, Scripta Metall. **V22**, 1988, pg. 1131.

20. C. McCullough, J.J. Valencia, C.G. Levi, R. Mehrabian, Acta Metall. **V37**, 1989, pg. 1321.

21. L.A. Willey, H. Margolin, *Metals Handbook*, **V8**, 1973, pg. 264.

22. R. Struchor, J.C. Williams, W.A. Soffa, Met Trans A. **V19A**, 1988, pg. 225.

23. J.L. Murray, Met Trans A. **V19A**, 1988, pg. 243.

24. Y-W. Kim, F.H. Foes, *High Temperature Aluminides and Intermetallics*. Edited by Y-W. Kim *et al*, TMS, 1990, pg. 465.

25. D.Y. Seo, PhD Dissertation. Michigan State University, 1999, pg. 49.

26. M. Yamaguchi, Y. Umakoshi, Progress in Materials Science. **V34**, 1990, pg. 13.

27. M. Yamaguchi, Y. Umakoshi, Progress in Materials Science. **V34**, 1990, pg. 24.

28. C.R. Feng, D.J. Michel, C.R. Crowe, Scripta Metall. **V22**, 1988, pp. 1481-1488.

29. C.R. Feng, D.J. Michel, C.R. Crowe, Scripta Metall. **V23**, 1989, pp. 1135-1140.

30. Y-W. Kim, Acta Metall., **V40**, No. 6, 1992, pp. 1121-1134.

31. M. Yamaguchi, Metals and Technology. **V60**, 1990, pg. 34.

32. Y. Yamabe, K. Sugawara, M. Kikuchi, *Proceedings. Of 1990 Tokyo Meeting, Japan Institute of Metals. Sendia: The Japan Inst. of Metals.* 1988, pg. 409.

33. Y.S. Yang, S.K. Wu, Sripta Metall., **V24**, 1990, pp. 1801-1806.

34. J.J. Valencia, C. McCullough, C.G. Levi, R. Mehrabian, Scripta Metall. **V21**, 1987, pp. 1341-1346.

35. C.R. Feng, D.J. Michel, C.R. Crowe, *MRS Meeting, Proceedings*, 1998.

36. M. Yamaguchi, Y. Umakoshi, Progress in Materials Science. **V34**, 1990, pg. 66.

37. Y-W. Kim, *High Temperature Ordered Intermetallic Alloys IV.* TMS, 1991, pp. 777-793.

38. S-C. Huang, D.S. *Shih, Microstructure/Property Relationships in Titanium Aluminides and Alloys.* Edited by Y-W. Kim, R.R. Boyer, TMS, 1990, pp. 105-122.

39. S-C. Huang, E.L. Hall, *High Temperature Ordered Intermetallic Alloys III*, TMS, 1990, pp. 373-383.

40. J.D. Bryant, S.L. Kampe, L. Christodoulu, Met. Trans. A, **V22**, 1991, pg. 447.

41. S.L. Kampe, J.D. Bryant, L. Christodoulu, Met, Trans, A, **V22**, 1991, pg. 2009.

42. M.E. Hyman, C. McCullough, J.J. Valencia, C.G. Levi, R. Mehrabian, Met. Trans. A, **V20A**, 1989, pp. 1847-1859.

43. Y. Umakoshi, T. Nakano, Acta Metall. Mater. **V41**, 1993, pp. 1155-1161.

44. C. Koeppe, A. Bartels, J. Seeger, H. Mecking, Metall. Trans. **V24A**, 1993, pg. 1795.

45. S-C. Huang, D.S. Shih, in Y.W. Kim, R.R. Boyer, *Titanium Aluminides and Alloys*, TMS, 1990, pg.105.

46. V.K. Vasudevan, S.A. Court, P. Kurath, H.L. Fraser, Scripta Metall. **V23**, 1989, pg. 467.

47. R. Wagner, F. Appel, B. Dogan, P.J. Ennis, U. Lorenz, J. Mullauer, H.P. Nicolai, W. Quadakkers, L. Singheiser, W. Smarsly, W. Vaidya, K. Wurzwallner, *Gamma Titanium Aluminides.* Edited by Y-W. Kim *et al*, 1995, pg. 387.

48. J. Klumpfert, Y-W. Kim, D.M. Dimiduk, Mat. Sci. and Eng. A. **VA192/193**, 1995, pg. 465.

49. H. Clemens, W. Glatz, F. Appel, Scripta Mat. **V35**, 1996, pg. 429.

50. H. Oikawa, Mat. Sci. and Eng A. **V153**, 1992, pp. 427-432.

51. H.A. Lipsitt, D. Shechtman, T. Schafrik, Met Trans. A. **V6**, 1975, pg. 1991.

52. M. Yamaguchi, Y. Umakoshi, Progress in Materials Science. **V34**, 1990, pg. 1.

53. S.L.M. Sastry, H.A. Lipsitt, Met Trans A. **V8**, 1977, pg. 299.

54. T. Kawabata, T. Kanai, O. Izumi, Acta Metall. **V33**, 1985, pg. 1355.

55. S-C. Huang, E. Hall, *High Temperature Ordered Intermetallic Alloys III.* Edited by C.T. Lui *et al.* **Vol. 133**, 1989, pg. 133.

56. J.W. Christian, D.E. Laughlin, Acta Metall. **V36**, 1988, pg. 1617.

57. C.T. Liu, A.I. Taub, N.S. Stoloff, C.C. Koch, *High-Temperature Ordered Intermetallic Alloys III.* Edited by C.T. Lui *et al.* **Vol. 133**, 1989, p 189.

58. J.W. Christian, D.E. Laughlin, Acta Metall. **V36**, 1988, pg. 1617.

59. M.H. Yoo, C.L. Fu, J.K. Lee, *High Temperature Ordered Intermetallic Alloys III.* Edited by C.T. Lui *et al.* **Vol. 133**, 1989, pg. 189.

60. C.R. Feng, D.J. Michel, C.R. Crowe, Scripta Metall. **V23**, 1989, pp. 241-246.

61. J. Beddoes, L. Zhao, P. Au, D. Dudzinski, J. Triantafillou, *Structural Intermetallics.* Edited by M.V. Nathal *et al.* 1997, pp. 109-118.

62. D. Shechtman, M.J. Blackburn, Met. Trans. A. **V 5**, 1974, pp. 1373-1381.

63. R.W. Evans, B. Wilshire, *Introduction to Creep. The Institute of Materials*, 1993.

64. T.R. Bieler, D.Y. Seo, T.R. Everard, P.A. McQuay, *Creep Behavior of Advanced Materials for the 21st Century.* Edited by R.S. Mishra *et al.* TMS, 1999, pp. 181-196.

65. B.D. Worth, J.W. Jones, J.E. Allison, Met. Mat. Trans A. **V26A**, 1995, pp. 2947-2959.

66. Y. Nagae, K. Maruyama, H. Oikawa, Mat. Sci. and Eng. A. **V213**, 1996, pp. 32-36.

67. D.Y. Seo, T.R. Bieler, D.E. Larsen, *Advancments. In Science. and Tech. Of Titanium Alloy Processing.* Edited by I. Weiss *et al.* TMS, 1997, pp. 603-622.

68. B. Skrotzki, *Gamma Titanium Aluminides.* Edited by Y-W. Kim *et al.* 1999, pp. 619-626.

69. B.D. Worth, J.W. Jones, J.E. Allison, Met. Mat. Trans A. **V26A**, 1995, pp. 2961-2972.

70. K. Maruyama, T. Takahashi, H. Oikawa, Mat. Sci. and Eng. A. **V153A**, 1992, pp. 433-437.

71. I. Haurie, L. Christodoulou, I.J. Perrin, A. Partridge, *Gamma Titanium Aluminides.* Edited by Y-W. Kim *et al.* 1999, pp. 725-731.

72. B.D. Worth, J.W. Jones, J.E. Allison, W.E. Dowling, Jr., *Properties and Microstructures of High Temperature Materials.* Edited by Y-W. Kim, R.R. Boyer, TMS, 1993.

73. C. Tonnes, J. Rosler, R. Baumann, M. Thumann, *Structural Intermetallics.* Edited by R. Darolia *et al*, TMS, 1993, pp. 241-245.

74. K.J. Hemker, M. Lu, M. Zupan, *Structural Intermetallics.* Edited by M.V. Nathal *et al*, 1997, pp. 147-156.

75. Z. Jin, T.R. Bieler, Phil. Mag. A. **V71**, No. 5, 1994, pp. 925-947.

76. B. Skrotzki, M. Unal, G. Eggeler, Scripta Mat. **V39**, 1998, pp. 1023-1029.

77. T. Kawabata, T. Tamura, O. Izumi, Metall. Trans. A, **V24A**, 1993, pg. 141.

78. A. Menand, A. Huguet, A. Nerac-Partiax, Acta. Mater. **V44**, 1996, pg. 4729.

79. A. Denquin, S. Naka, A. Huguet, A. Menand, Scripta Metall. Mater., 28, 1993, pg 1131.

80. T. Kawabata, T. Abumiya, O. Izumi, Acta Metall. Mater. **V40**, 1992, pg. 2557.

81. F. Appel, U. Christoph, R. Wagner, *Mat. Res. Soc. Symp. Proc.* **V460**, 1997, pp. 77-82.

82. W.E. Dowling, Jr., W.T. Donlon, Scripta Metall. **V27**, 1992, pp. 1662-1667.

83. R. Ayer, R. Ray, J.C. Scanlon, Scritpa Metal. Mater. **V26**, 1992, pp. 1337-1342.

84. Lausanne Electron Microscopy Homepage. [Online] Available http://cimewww.epfl.ch/, May, 2000.

85. Practical Electron Microscopy of Materials Science, J.W. Edington, Phillips, 1974.

86. Transmission Electron Microscopy; D.B. Williams, C.B. Carter. Vol. 1-4, (1996). Plenum Press, New York.

87. Physical Metallurgical Principles, R.E. Reed-Hill, R. Abbaschian.3rd ed.(1992) PWS-Kent Publishing, Boston.